科学通报 2026 年 第 71 卷 第 11 期: 2387 ~ 2407
超导薄膜与器件专题 评 述
《中国科学》杂志社 SCIENCE CHINA PRESS

钇钡铜氧薄膜与约瑟夫森结研究进展

张济全[1], 陈赋聪[1*], 马小平[1], 乔丹[2], 王宇彤[1], 杨景婷[3], 冯中沛[3], 柏中华[1], 熊沛雨[3], 王家晓[1], 李春光[1], 杨槐馨[1], 李潜[1], 田士兵[1], 高翔[2], 王越[4], 王旭[1*], 袁洁[1], 朱北沂[1], 金魁[1]

1. 中国科学院物理研究所, 北京 100190
2. 北京理工大学网络空间安全学院, 北京 100081
3. 松山湖材料实验室, 东莞 523808
4. 北京大学物理学院, 北京 100871
* 联系人, E-mail: fucong@iphy.ac.cn; risingsunwx@iphy.ac.cn

2025-10-01 收稿, 2026-01-20 修回, 2026-01-21 接受, 2026-01-22 网络版发表
国家自然科学基金青年科学基金(A类)(12225412)、中国科学院超导专项(SCZX-0102, SCZX-0201)、中国科学院稳定支持基础研究领域青年团队项目(2022YSBR-048)、国家自然科学基金(U23A6015, 52588301)和国家重点研发计划(2022YFA1603900)资助

摘要 钇钡铜氧($YBa_2Cu_3O_{7-\delta}$, YBCO)薄膜与约瑟夫森结的可控制备是高温超导机理和电子学器件研究的基础. 随着薄膜制备技术的进步, YBCO薄膜的超导转变温度、临界电流密度、表面平整度、大面积制备能力与均匀性不断提升. 然而, 相比于单晶, YBCO薄膜的超导转变温度、微波表面电阻仍有提高空间. 通过衬底应力调制、缓冲层引入与超晶格构建等界面控制手段, 可有效抑制薄膜孪晶, 进而调控其超导电性和电子结构. 这为揭示高温超导机理及提升薄膜与约瑟夫森结性能提供了新的研究路径. 高温超导电子学器件的产业化有赖于约瑟夫森结/结阵列的性能、规模与稳定性的进一步提升. YBCO约瑟夫森结的主要类型包括双晶结、台阶结、斜边结、台阶SNS结及聚焦氦离子束(focused helium ion beam, He-FIB)辐照结等. He-FIB技术凭借其纳米级加工精度和高自由度, 能够实现结参数的精准调控和大规模结阵列制备. 本文系统阐述了YBCO薄膜和约瑟夫森结的研究进展, 并展望其未来发展趋势.

关键词 高温超导, 钇钡铜氧, 薄膜, 约瑟夫森结, 电子学器件, 聚焦氦离子束

高温超导机理是当今物理学最具挑战性的前沿问题之一, 高温超导薄膜是研究机理问题的重要载体; 而高温超导电子学器件在雷达通信、生物医学、地球物探、精密测量等前沿领域也极具应用潜力, 其主要基于高温超导薄膜以及约瑟夫森结. 中国科学院物理研究所赵忠贤团队[1]与美国休斯顿大学朱经武团队[2]分别于1987年发现的钇钡铜氧($YBa_2Cu_3O_{7-\delta}$, YBCO)高温超导体, 是众多高温超导材料的典型代表. YBCO具有超导转变温度高(T_c>90 K)[3]、超导能隙大(最大能隙Δ_0~30 meV)[4]、微波表面电阻(R_s≈0.2 mΩ@77 K, 10 GHz)[5]低、薄膜的临界电流密度高(J_c~5 MA/cm^2@77 K)[6]、制备方法灵活等优势. 因此, YBCO薄膜与约瑟夫森结是高温超导机理和电子学器件研究的可靠载体.

高温超导YBCO薄膜的机理和应用研究涉及临界转变温度T_c[7~9]、上临界磁场H_{c2}[10,11]、相位刚度ρ_s[12,13], 临界电流密度J_c[14~17]、微波表面电阻R_s[18~21]、正常态电子结构演化[22,23]、薄膜生长机制[24~27]等多个方面. 高温超导机理研究和约瑟夫森结制备对YBCO薄膜物性, 如超导电性、掺杂水平、结构、表面、均匀性等都有针对性要求, 前者主要关注薄膜物性的演化机制, 后者追求薄膜性能的极致. 基于薄膜的高温超导

引用格式: 张济全, 陈赋聪, 马小平, 等. 钇钡铜氧薄膜与约瑟夫森结研究进展. 科学通报, 2026, 71: 2387–2407
Zhang J-Q, Chen F-C, Ma X-P, et al. Research progress on $YBa_2Cu_3O_{7-\delta}$ thin films and Josephson junctions (in Chinese). Chin Sci Bull, 2026, 71: 2387–2407, doi: 10.1360/CSB-2025-5615

© 2026《中国科学》杂志社

机理研究正面临认知深化的关键阶段，面向约瑟夫森结制备的薄膜质量仍有提升空间，亟需在薄膜制备技术和研究范式上实现创新突破. 研究人员前期通过YBCO的约瑟夫森效应发现YBCO主要具有d波配对对称性($\Delta = \Delta_0\cos(2\phi)$, 其中$\phi = \arctan\left(\frac{k_y}{k_x}\right)$, k_y和k_x为载流子动量的分量)[28]. 目前, YBCO约瑟夫森结的发展目标是面向液氮温区电子学器件的高性能、稳定性与阵列化能力等. 制备YBCO约瑟夫森结的主要挑战在于构建纳米尺度的约瑟夫森结势垒区, 其宽度受限于YBCO相干长度ξ(77 K)≈30 Å. 因此, 为实现YBCO约瑟夫森结从实验室走向应用，不仅需要发展先进的结制备手段和稳定的高质量薄膜制备技术作为保障，还需要明晰结区微观结构和约瑟夫森结性能的构效关系，从而在深入理解物理机制的基础上进行持续优化.

本文主要阐述YBCO薄膜和约瑟夫森结的制备、物理与应用. 首先, 介绍YBCO薄膜的基本物性、制备技术、机理研究的最新进展，以及中国科学院物理研究所与松山湖材料实验室联合团队研制的高质量YBCO薄膜; 其次, 介绍YBCO约瑟夫森结的基本原理、超导电子学应用、主流制备技术，以及单结和结阵列性能的研究进展; 最后，对YBCO薄膜与约瑟夫森结的物性研究和应用前景进行总结与展望.

1 薄膜物理与应用

1.1 基本物性

YBCO是$ReBa_2Cu_3O_{7-\delta}$(ReBCO，Re=稀土元素，如Y、Gd、Dy、Nd等, $0\leqslant\delta\leqslant1$)家族的一员，其晶胞由3个畸变的钙钛矿结构组成，包括Y层、BaO层、一对间距约为3.2Å的CuO_2超导平面与提供空穴载流子的Cu-O链(氧原子数为$1-\delta$). 当Cu-O链的氧含量不足50%(δ>0.5)时, YBCO为四方结构, a=b≈3.86 Å; 当Cu-O链的氧含量补充至50%以上(δ<0.5)时, YBCO转变为正交相, a≈3.82 Å, b≈3.89 Å; 随着Cu-O链的氧含量上升, c轴晶格常数逐渐由11.82 Å下降为11.68 Å，如图1(a)所示. CuO_2平面的层状结构导致了YBCO在c方向与ab面内的各向异性: a方向和b方向的临界电流密度和电导率高于c方向. YBCO在ab面内也存在各向异性，这一差异源于Cu-O链沿b轴方向周期性排列形成的额外载流子输运通道.

当δ≈0.1时，YBCO的超导转变温度最高，即达到最佳掺杂水平，此时单晶的T_c(磁化率测量)可达93.2 K[3]，展宽ΔT_c<0.25 K；薄膜的T_{c0}(电输运测量)则可以达到92.1 K[18]. 其他超导参量的典型值如图1(b)与表1所示，包括上临界磁场H_{c2}[10,11,29]、下临界磁场H_{c1}[30]、相干长度ξ[31]、穿透深度λ[12,32,33]、临界电流密度J_c等. 为精确测量出最佳掺杂YBCO极高的上临界场，Sekitani等人[10,11]开发了非接触式射频传输技术用于产生高达~400 T的短脉冲超强磁场，得到$H_{c2\|c}$(0 K)≈120 T, $H_{c2\perp c}$(0 K)≈250 T. Grissonnanche等人[29]指出H_{vs}(0 K)=H_{c2}(0 K)，并进一步通过拟合$H_{vs}(T)$得到H_{c2}(0 K)，其中$H_{vs}(T)$为融化场. 当外加磁场逐渐提高到$H_{vs}(T)$，磁通融化为液态，此时电阻将从零开始迅速上升. YBCO面内相干长度$\xi_{ab} \ll l$，l为平均自由程，可以使用$\Phi_0/2\pi\xi_{ab}^2 = \mu_0 H_{c2\|c}$与$\Phi_0/2\pi\xi_c\xi_{ab} = \mu_0 H_{c2\perp c}$计算相干长度.

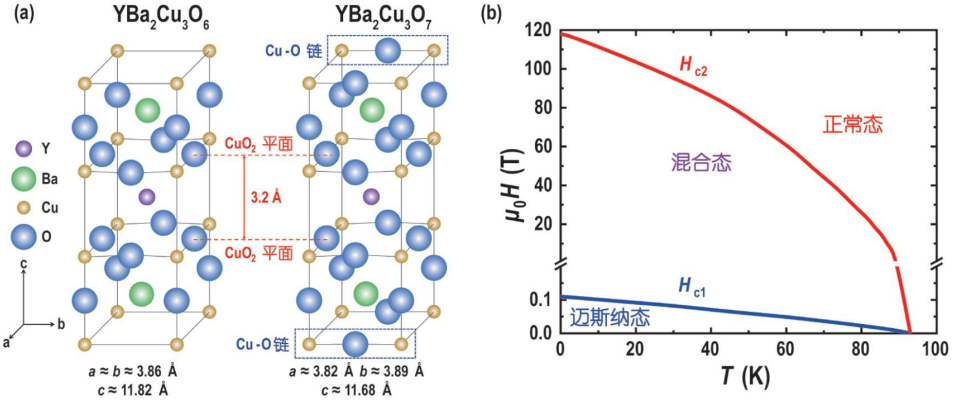


图 1 YBCO的结构与基本超导电性. (a) YBCO结构: Cu-O链氧含量过半时从四方相变为正交相; (b) 最佳掺杂YBCO的磁场(H)-温度(T)相图

Figure 1 Structure and basic superconductivity of YBCO. (a) The structure of YBCO. It transforms from the tetragonal phase to the orthorhombic phase when the oxygen content in the Cu-O chain exceeds half; (b) magnetic field (H)-temperature (T) phase diagram of optimal doped YBCO

表 1 最佳掺杂YBCO的超导特性[3,10~12,18,29~33]a)

Table 1 Superconducting properties of optimal-doped YBCO[3,10–12,18,29–33]

	方向	T_c	ξ (0 K)	λ (0 K)	H_{c2} (0 K)	H_{c1} (0 K)
单晶	*ab*	93.2 K	10~15 Å	100~160 nm	n/a	0.02 T
	c		n/a	1060 nm	115 T	0.11 T
薄膜	*ab*	92.1 K	16.6 Å	180 nm	250 T	n/a
	c		8 Å	n/a	120 T	n/a

a) n/a表示缺少准确数据

1.2 薄膜制备技术

YBCO薄膜可以按照膜厚t分为三类: (1) t > 300 nm: T_c > 90 K, 接近单晶水平. 广泛应用于滤波器等微波无源器件中, 要求T_c、J_c、t等性质在两到三英寸的面积内均匀分布, 微波表面电阻R_s尽量小. (2) 10 nm < t < 300 nm: T_c随膜厚降低而下降至90~85 K. 用于制作约瑟夫森结, 要求具有高T_c、高掺杂水平p(与Cu-O链氧含量正相关, 见1.3节)与较小的表面粗糙度R_q. (3) t < 10 nm: T_c随膜厚降低出现明显下降, 与薄膜制备过程相关. 可用于制作纳米线单光子探测器和超晶格, 主要挑战在于保持较高T_c.

YBCO薄膜的主要制备手段及其优缺点如下: (1) 脉冲激光沉积[34], 其薄膜沉积速率大范围可调, 但薄膜生长通量存在横向不均匀性; (2) 磁控溅射[35], 可用于生长均匀的大面积薄膜或高T_c的YBCO超薄膜, 但生长速率较缓慢; (3) 蒸发与分子束外延[36], 可生长高结晶性的YBCO超薄膜, 但生长速率缓慢; (4) 金属有机化学气相沉积[37], 可快速均匀外延生长高结晶性的大面积YBCO薄膜, 但难以控制较薄的YBCO薄膜的生长; (5) 液相或固相方法[38], 可快速生长YBCO厚膜或带材, 但难以控制较薄的YBCO薄膜的生长.

常用于生长YBCO薄膜的衬底包括具有ABO_3型结构的$DyScO_3$、$SrTiO_3$、$La_{0.18}Sr_{0.82}Al_{0.59}Ta_{0.41}O_3$、$NdGaO_3$、$LaAlO_3$等, 以及低微波损耗、低成本的MgO等, 它们与YBCO的晶格匹配性如图2(a)所示. YBCO薄膜的气相法制备可以参照电化学法给出的YBCO热力学稳定性相图(图2(b))来理解[39]. 生长c取向的YBCO薄膜需要合适的温度和氧压, 过高的生长温度会导致YBCO分解为其他化合物, 较低的生长温度会导致成相变差, 也会促使YBCO薄膜沿a方向生长[24]. 因此, 通常先将薄膜生长条件设置在$YBa_2Cu_3O_6$的不稳定边界附近, 沉积出Cu-O链处于缺氧状态的高结晶性、c取向四方相YBCO薄膜, 再通过降温退火使Cu-O链的氧含量达到所需值.

YBCO薄膜退火面临着两个主要技术问题, 第一个问题是: 在制备δ < 0.5的YBCO薄膜的退火过程中, YBCO从退火前的四方相转变为正交相, 氧原子将从两个方向补充, 形成夹角90°孪晶, 影响了输运、电子结构表征结果的本征性, 也阻碍了物理机制与应用性能关联的建立. 针对该问题, 人们通常采用具有面内正交性的衬底, 如斜切$SrTiO_3$(100)[25](如图2(c)所示)、MgO(110)[26]等, 这类衬底的应力促使氧原子在退火时沿单一方向补充入铜氧链, 非孪晶率可以达到90%以上. 第二个技术问题是: 退火过程中氧原子需要垂直于YBCO薄膜表面向内部输运, 导致薄膜上、下层Cu-O链氧含量不均匀, 无法实现均匀的掺杂, 导致薄膜及后续约瑟夫森结的性能与工艺稳定性欠佳. 针对该问题, 在采用分子氧的情况下, 人们通常对退火时的氧气压强和降温曲线进行精确控制以实现均匀掺杂, 并结合赝能隙打开温度T^*、霍尔载流子浓度n_H[14]或晶格常数c[40]判断YBCO的掺杂水平. 另一方面, 更具有活性的退火氧源可能提高Cu-O链的补充效率, 如臭氧[41]与原子氧[35]的等效压强更高, 氧等离子则能够增强a取向YBCO薄膜的结晶性[42].

此外, 薄膜先进制备技术的开发能够给YBCO薄膜物理与应用研究带来新动力. 比如在脉冲激光沉积中, 通过交替烧蚀不同靶材, 辅以可编程移动掩膜板、衬底原子级平整表面原位处理并使用反射式高能电子衍射(reflection high-energy electron diffraction, RHEED)实时监测生长过程, 实现组合薄膜生长[43]、界面精确控制或两者结合, 界面控制包括缓冲层、保护层与超晶格(如图2(d)所示)等.

1.3 YBCO薄膜物性近期研究进展

结合低温与强磁场技术, 基于不同掺杂YBCO单晶的输运和谱学研究结果, 物理学家已总结出了YBCO的温度T-掺杂p相图, 如图3(a)所示: 在欠掺杂区间

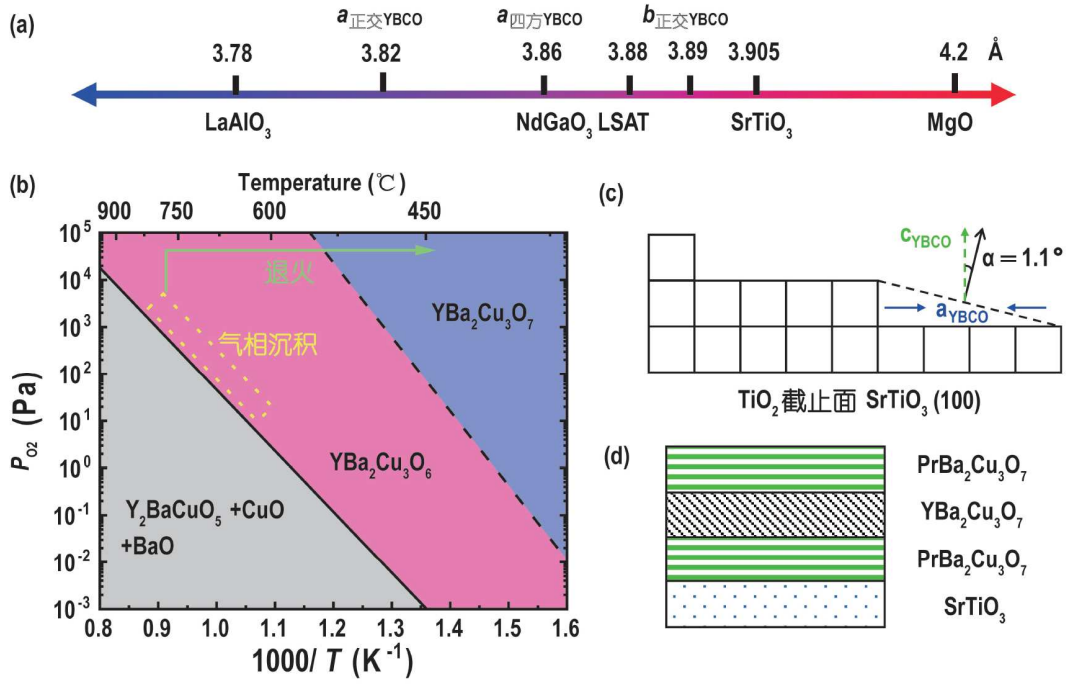


图 2 YBCO薄膜制备技术. (a) 常用衬底类型与晶格匹配性, LSAT是$La_{0.18}Sr_{0.82}Al_{0.59}Ta_{0.41}O_3$的简写; (b) 气相沉积原理: 生长条件设置在$YBa_2Cu_3O_6$的相稳定边界附近以提高结晶性, 最高$T_c$通常使用提高氧压、设计降温曲线的方式实现; (c) 一种去孪晶技术: 在处理出单一TiO_2截止面的斜切$SrTiO_3$衬底上, 垂直于台阶方向成为YBCO薄膜a轴的择优取向; (d) 在$SrTiO_3$衬底上生长的$PrBa_2Cu_3O_7$/YBCO/$PrBa_2Cu_3O_7$超晶格示意图

Figure 2 Preparation techniques of YBCO thin films. (a) Common substrate types and lattice matching. LSAT is the abbreviation of $La_{0.18}Sr_{0.82}Al_{0.59}Ta_{0.41}O_3$. (b) Principle of vapor deposition. The growth condition is set near the phase stability boundary of $YBa_2Cu_3O_6$ to enhance crystallinity, and the optimal T_c is achieved by increasing oxygen pressure and reducing temperature during annealing. (c) A detwinning technique. On a vicinal $SrTiO_3$ substrate with a single TiO_2 termination, the direction perpendicular to the step terrace becomes the preferred orientation of the a-axis of the YBCO film. (d) A schematic diagram of $PrBa_2Cu_3O_7$/YBCO/$PrBa_2Cu_3O_7$ superlattice grown on $SrTiO_3$ substrate

($0.05 < p < 0.16$), 电荷密度波、自旋密度波等有序态与超导电性共存[44]; 最佳掺杂处($p = 0.16$), 最高T_c> 93 K; 过掺杂区间($0.16 < p < 0.194$)中, 电荷密度波与赝能隙相继消失[45], 电子有效质量增强[46]. 其中, 掺杂水平p取决于铜氧链的氧含量$1-\delta$, 与晶格常数c负相关[40]. YBCO的上临界磁场随掺杂的变化呈现出双峰值特征, Grissonnanche等人[29]认为该特征分别源于电荷序和自旋序导致的费米面重构, 如图3(b)所示. 相比于上临界磁场, YBCO的下临界磁场很小, 基于不同测量手段得到的结果差别很大, 因此仅展示不同掺杂单晶的典型值. 单晶的下临界场也被用于计算相位刚度ρ_s(0 K), 如图3(c)所示. 相比于YBCO单晶, 厚度、衬底界面、多层异质结构或三者的结合为YBCO薄膜的高温超导机理研究提供了更多的调制维度, 为超导参数与电子结构的演化规律研究带来了新的范式, 研究者得以在YBCO薄膜中观察到不同于单晶的物性.

研究铜氧面层数受限情况下的超导电性是物理学界探索高温超导电性起源的途径之一. 目前报道的YBCO超薄膜T_c一般低于块体, 且随膜厚减小而下降, 这一现象在YBCO晶胞层数小于5时较为显著[47]. 相对照, 解理出的单个$Bi_2Sr_2CaCu_2O_{8+\delta}$晶胞却能够保持块体的超导电性[48]. 图3(d)总结了YBCO超薄膜T_c与膜厚t的依赖关系. 在薄膜仅具有YBCO单层结构情况下, 衬底的晶格匹配度对于YBCO超薄膜的T_c具有重要影响, 如Zhai等人[49]在构成压缩应力的$LaAlO_3$衬底上生长的2个晶胞厚YBCO薄膜T_c~20 K, 但在构成拉伸应力的$SrTiO_3$衬底上生长的2个晶胞厚YBCO薄膜则不超导, 且同等厚度(小于7 nm)的YBCO/$LaAlO_3$薄膜的T_c均高于YBCO/$SrTiO_3$薄膜的T_c. 这些ABO_3型结构的衬底表面一般处于AO与BO_2两种截止面混杂的情况, 但研究人员借助高温退火与化学刻蚀手段, 已能够将表面处理为单一截止面[50]. 其中, $SrTiO_3$的截止面影响YBCO

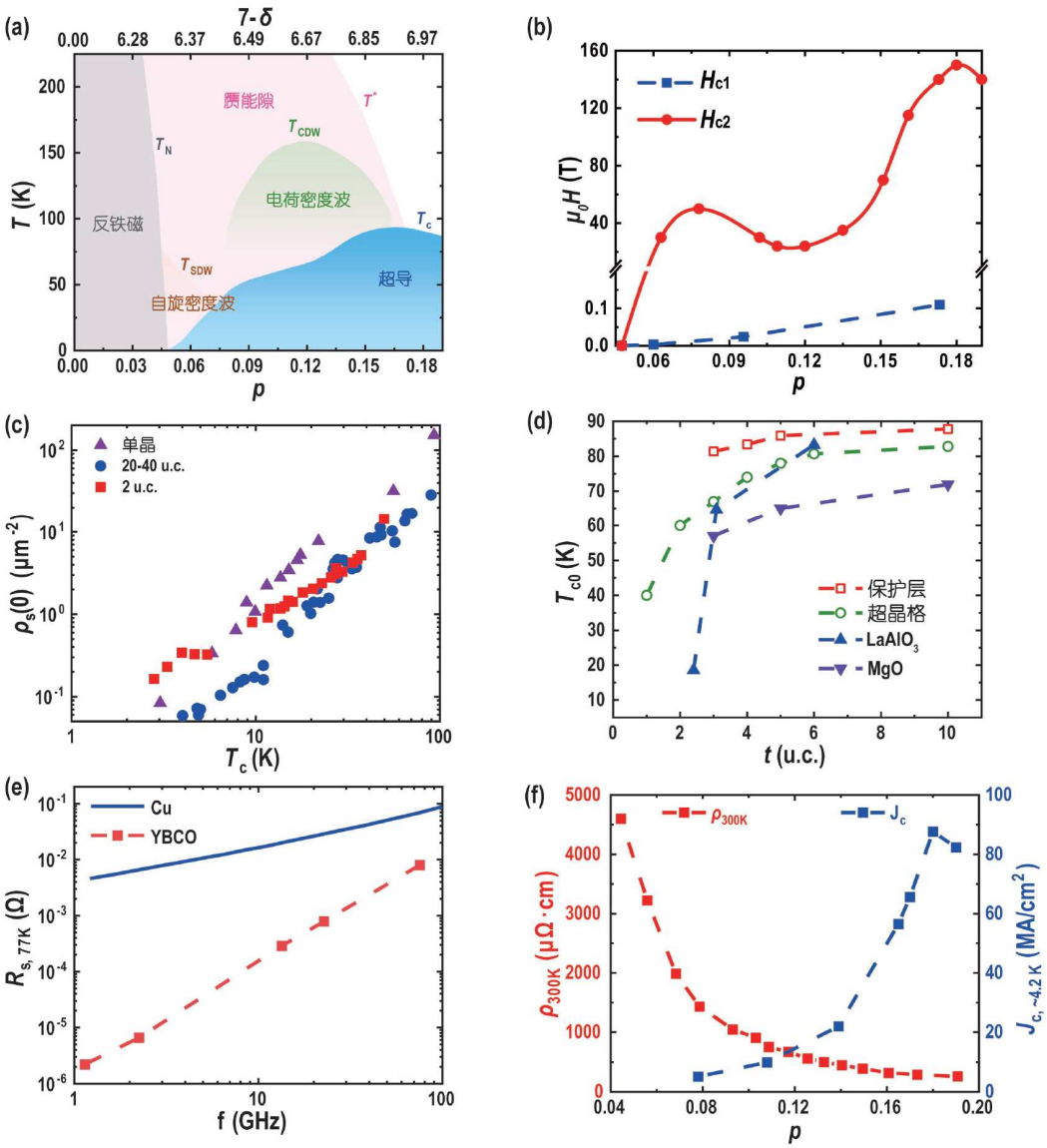


图 3 YBCO的物性. (a) YBCO的温度(T)-掺杂(p)电子态相图; (b) YBCO临界场(H_{c2}, H_{c1})-掺杂(p)相图, H_{c2}来源于文献[29], H_{c1}来源于文献[30,65]; (c) YBCO相位刚度(ρ_s)-掺杂(p)相图[13]; (d) YBCO超薄膜T_c-膜厚(t)依赖关系, 保护层表示在$SrTiO_3$衬底上生长的非晶YBCO保护的薄膜[47], 超晶格表示$PrBa_2Cu_3O_7$/YBCO/$PrBa_2Cu_3O_7$[8], $LaAlO_3$[49]与MgO[9]表示分别在这两种衬底上生长的单层YBCO薄膜; (e) $f \in (1, 100)$ GHz区间内金属Cu[66]与YBCO[5]的微波表面电阻(R_s)对比; (f) YBCO正常态电阻率(ρ_n)[64]与临界电流密度(j_c)[14,67]的掺杂(p)依赖性

Figure 3 Physical properties of YBCO. (a) Temperature (T) vs. doping (p) electronic phase diagram of YBCO. (b) Critical field (H_{c2}, H_{c1}) vs. doping (p) phase diagram of YBCO. H_{c2} is from Ref. [29], and H_{c1} is from Refs. [30,65]. (c) Phase stiffness (ρ_s) vs. doping (p) phase diagram of YBCO[13]. (d) T_c of YBCO ultrathin film as a function of film thickness (t). The protective layer represents the amorphous YBCO-protected film grown on $SrTiO_3$ substrate[47], the superlattice represents $PrBa_2Cu_3O_7$/YBCO/ $PrBa_2Cu_3O_7$[8], $LaAlO_3$[49] and MgO[9] represent the single-layer YBCO films grown on these two substrates, respectively. (e) Comparison of microwave surface resistance (R_s) of metal Cu[66] and YBCO[5] within the (1, 100) GHz range. (f) Doping (p) dependence of normal state resistivity (ρ_n)[64] and critical current density (j_c)[14,67] of YBCO

晶胞的生长顺序: Schlepütz等人[51]通过采用原子与薄膜位移约束的差分图(phase-retrieval direct-method difference map using the constraints of atomicity and film shift, DCAF)发现$SrTiO_3$的SrO截止面与YBCO的CuO_2平面或Cu-O链相连, 而TiO_2截止面与YBCO的Y层或BaO层相连, 但截止面与YBCO超薄膜T_c的关联尚不清晰. 为了在YBCO超薄膜中实现更高的T_c, 实验人员通常原位室温生长非晶YBCO或其他氧化物材料的保护层, 用于防止或减轻加工、表征过程中YBCO超薄膜的超导电性退化. Lyatti等人[47]使用磁控溅射在$SrTiO_3$衬

底上生长YBCO超薄膜，其中非晶YBCO保护下的3个晶胞厚YBCO薄膜的T_{c0}高达80 K，而非晶YBCO保护下的5个晶胞厚YBCO薄膜J_c(77 K) = 2.5 MA / cm^2. 研究人员也通过界面控制技术逐步了解了导致YBCO超薄膜T_c下降的可能因素：Terashima等人[7]和Matsuda等人[8]生长了YBCO层数最低为1的$PrBa_2Cu_3O_7$/YBCO/$PrBa_2Cu_3O_7$超晶格，前者发现空穴载流子降低导致了YBCO超薄膜T_c下降，而$PrBa_2Cu_3O_7$能够提供空穴载流子; Garcia-Barriocanal等人[52]在$SrTiO_3$/YBCO超晶格输运研究中发现无序水平上升是YBCO超薄膜T_c下降的重要因素.

探究T_c与相位刚度$\rho_s(0\ \mathrm{K}) = \lambda^{-2}(0\ \mathrm{K})$的标度关系也是理解高温超导机理和微波表面电阻$R_s$的重要途径之一，如图3(c)所示. YBCO超薄膜较大的T_c调控范围使其成为研究T_c与ρ_s(0 K)标度关系的良好载体. Hetel等人[13]使用互感线圈测量了2个晶胞厚的Ca掺杂YBCO的超晶格($PrBa_2Cu_3O_7$/Ca-YBCO/$PrBa_2Cu_3O_7$)的交流磁化率，总结出$T_c > 20$ K时，YBCO的单晶、单层薄膜与2晶胞超晶格都符合$T_c \propto \rho_s(0)^{0.5}$三维量子临界标度律，但2晶胞YBCO超晶格在$T_c < 20$ K时满足$T_c \propto \rho_s(0)$二维量子临界标度律; Fête等人[53]则通过静电场调控技术诱导YBCO超薄膜的空穴载流子变化，并通过测量J_c(4.2 K)提取出$T_c^{1.91} \propto \rho_s(0)$的标度律. 值得注意的是，YBCO单晶的$\rho_s(0)$显著高于YBCO薄膜.

研究人员将YBCO薄膜技术与斜边结技术(见第2.3.4节)相结合，通过相位敏感技术确定了YBCO的超导配对对称性. Smilde等人[54]将YBCO/Au/Nb斜边结加工成具有交替垂直刻面的锯齿形(zigzag junctions)，通过测量并拟合$I_c(H)$曲线验证YBCO的序参量主要满足$d_{x^2-y^2}$对称性，且*is*分量占比小于1%. Kirtley[55]等人在斜切$SrTiO_3$上制备了具有85%非孪晶比例的YBCO最佳掺杂薄膜，加工出一系列具有两组YBCO/Nb斜边结、夹角连续变化的环形阵列，通过扫描SQUID测量环内磁通，发现$\Delta_s / \Delta_{d_{x^2-y^2}} \sim -0.1$，说明沿*b*轴的能隙比沿*a*轴的能隙高出20%，id_{xy}、*ip*、*is*的占比均小于2.5%.

在电输运和电子结构方面，最佳掺杂YBCO薄膜的正常态电阻率与温度几乎呈线性关系：$\rho \approx \rho_0 + A_1 T$[56]，欠掺杂和最佳掺杂YBCO薄膜的线性电阻率现象只发生在赝能隙打开温度T^*以上[57]，而过掺杂YBCO薄膜中电阻率$\rho = \rho_0 + A_1 T + A_2 T^2$(见第1.4节). 不同掺杂YBCO薄膜电阻率的温度依赖性与单晶相似，但ρ_0和A_1强烈依赖于厚度大小[47]和衬底类型[58]. Whalberg等人[22]在处理出纳米微面(nano-facet)的MgO(110)衬底上生长YBCO非孪晶薄膜，发现10 nm厚YBCO欠掺杂薄膜在*a*方向的电荷密度波受到抑制，从而导致*b*方向的线性电阻率延伸至T^*以下. Solovjov等人[23]通过生长不同$PrBa_2Cu_3O_7$厚度的$PrBa_2Cu_3O_7$/YBCO双层结构和$PrBa_2Cu_3O_7$/YBCO/$PrBa_2Cu_3O_7$超晶格来调节$PrBa_2Cu_3O_7$磁性与YBCO超导电性的相互作用，从而改变了高温区域赝能隙$\Delta^*(T)$的温度依赖性. Yuan等人[59]在YBCO薄膜的赝能隙相中观测到了太赫兹三次谐波光谱强度对温度的二阶导数斜率变化，发现该信号可能源于电荷密度波或赝能隙中的向列序. 以上结果表明，界面能够显著调制YBCO薄膜的电子结构，为研究高温超导机理并改善应用性能提供了重要线索.

微波表面阻抗$Z_s(\omega) = R_s(\omega) + iX_s(\omega)$描述了超导材料在微波频段下的交流输运特征，其中，微波表面电阻R_s是主导超导滤波器损耗性能的关键参量. 在77 K，10 GHz下，YBCO薄膜的$R_s \approx 0.2$ mΩ，远低于同频段的铜(如图3(e)所示)，可以实现极低损耗、高频率选择性的高阶数超导滤波器，在通信、雷达、射电天文等领域获得广泛应用，具体可参阅文献[60]. YBCO薄膜的R_s主要取决于频率ω、穿透深度λ以及未配对的正常态电子的电导率$\sigma_n(T,\omega)$. 令$\sigma_s = \dfrac{1}{\mu_0\omega\lambda^2}$，有$R_s = \dfrac{\omega\mu_0\sigma_s}{2\left(\sigma_n^2+\sigma_s^2\right)}\left(\sqrt{1+\dfrac{\sigma_n}{\sigma_s}}-1\right)\times\left(\coth\left(\dfrac{t}{\lambda}\right)+\dfrac{\dfrac{t}{\lambda}}{\sinh^2\left(\dfrac{t}{\lambda}\right)}\right)$. 在滤波器所使用的$t > 300$ nm的YBCO薄膜中，膜厚修正因子$\coth\left(\dfrac{t}{\lambda}\right)+\dfrac{\dfrac{t}{\lambda}}{\sinh^2\left(\dfrac{t}{\lambda}\right)} \approx 1$. 因此当$\sigma_n \ll \sigma_s$时，有$R_s = \dfrac{\mu_0}{2}\omega^2\lambda^3\sigma_n$. Hosseini等人[5]测量了高纯度的YBCO单晶在1.14、2.25、13.4、22.7和75.3 GHz下的$R_s(T)$，其中R_s(77 K, 13.4 GHz) ≈ 0.29 mΩ，并指出T>65 K时，R_s/ω^2的偏差小于8%，符合$R_s \propto \omega^2$且σ_n与ω无关的理论预期. 在这一理论前提下，拆解得R_s(77 K) =

$e^2\omega^2 m_n^{*-1/2} n_s^{-3/2} n_n \tau_n = e^2\omega^2\lambda\cdot\left(\frac{n_n}{n_s}\right)\times\tau_n$，说明微波表面电阻正比于电子配对凝聚比例的倒数和正常态载流子散射率的倒数. 尽管目前薄膜制备经过了一系列优化，YBCO薄膜R_s的下限尚未达到. Face等人[61,62]使用离轴磁控溅射在具有CeO_2缓冲层的蓝宝石衬底上制备了厚度为350 nm的YBCO薄膜，其R_s(77 K, 8.1 GHz)≈0.21 mΩ; Honmac等人[20]在MgO(100)衬底上使用共蒸发技术制备的700 nm厚YBCO薄膜，测量了c方向外加磁场下的R_s，其中R_s(77 K, 21.8 GHz, 0T)≈1 mΩ. 在薄膜制备与后处理环节，Einfeld等人[63]认为薄膜内部的微观缺陷导致了电子-杂质散射率的增加，从而降低了R_s; Sato等人[21]发现引入钉扎中心$BaZrO_3$或$BaHfO_3$能够降低R_s; Takanashi等人[19]发现硅离子或中子辐照能够降低直流磁场环境下的R_s. 如前文所述，界面具有调制YBCO薄膜的T_c、载流子浓度与电子结构的能力，这其中蕴含着进一步降低YBCO薄膜R_s的可能.

在同等工艺参数的前提下，多种类型的约瑟夫森结I_c、R_n和YBCO的临界电流密度J_c、正常态电阻率ρ_n分别呈正关联. YBCO薄膜J_c与ρ_n的掺杂依赖性如图3(f)所示. Stangl等人[14]在使用脉冲激光沉积和化学溶液沉积YBCO薄膜中，通过表面镶银退火实现过掺杂，由于超导凝聚能的提升，J_c(5 K)将随着霍尔载流子浓度n_H提升而增大，最高可达拆对电流的1/5. 这一结果说明随着YBCO的Cu-O链氧含量增加，J_c会持续增加，而并非像T_c一样在最佳掺杂处饱和. ρ_n则随掺杂水平升高而下降[64]. 此外，影响YBCO薄膜J_c的因素包括纳米复合材料掺杂[17]和衬底晶格失配导致的大角度晶界等，然而它们处于介观尺度，无法对势垒区宽度仅为几纳米的YBCO约瑟夫森结形成稳定作用. 基于上述结论，约瑟夫森结I_c、R_n的提升需要YBCO薄膜的J_c、ρ_n在轻微欠掺杂到过掺杂间实现权衡.

1.4 中国科学院物理研究所与松山湖材料实验室联合团队的YBCO薄膜研制进展

中国科学院物理研究所与松山湖材料实验室联合团队(以下简称联合团队)使用脉冲激光沉积制备不同类型的高质量YBCO薄膜. 如图4(a)~(d)所示，联合团队自主研发了高致密度(实际密度达到理论密度98%以上)YBCO靶材，通过生长与退火条件优化，稳定制备了面向约瑟夫森结应用的小尺寸(10 mm×10 mm和5 mm×5 mm)薄膜，既能够实现T_{c0} > 87 K, p = 0.18的60个晶胞厚的过掺杂YBCO薄膜，也能够实现T_{c0} > 89 K的30个晶胞厚的最佳掺杂薄膜. 前者的电阻率可用$\rho=\rho_0+A_1T+A_2T^2$拟合，$\rho_0\approx 0$，且以相同工艺制备的7个、4个晶胞厚YBCO薄膜T_{c0} > 80 K，归一化电阻重合，证明薄膜杂质含量很低，Cu-O链的氧掺杂水平高且均匀. 此外，能够实现的最佳表面粗糙度R_q < 1 nm，颗粒物密度< 5个/(100 μm)^2，为He-FIB约瑟夫森结阵列(见第3节)的工艺稳定性奠定了基础. 联合团队自主研发了完全国产化的三光束脉冲激光共沉积系统，通过非接触式可翻转辐照加热系统与激光组件自动化扫描实现两英寸双面或单面YBCO薄膜的均匀生长，如图4(e), (f)所示. 其中，面向滤波器应用的YBCO薄膜单面最小R_s(77 K, 10 GHz) = 0.18 mΩ，达到国际领先水平.

2 约瑟夫森结制备与应用

2.1 约瑟夫森结基本原理

约瑟夫森效应是一种宏观量子效应，它是超导电子学应用的重要物理基础. 当两个超导体由一层薄的势垒层隔开(通常为氧化物薄膜或金属)，两个超导体的超导波函数仍然保持相位相干，库珀对仍可无阻穿过势垒层从而产生超导电流. 超导电流的值I_φ与两端超导体的相位差φ有关:

$$I_\varphi = I_c\sin\varphi, \tag{1}$$

其中，I_c是约瑟夫森结临界电流.

当两端超导体之间不存在电压降时，通过势垒层的电流为直流电流. 当存在电压降V时，相位差φ是与V相关的含时变量:

$$\frac{d\varphi}{dt}=\frac{2eV}{\hbar}. \tag{2}$$

当约瑟夫森结两端的电压是恒定电压时，相位差随时间线性变化，结上产生固定频率的交变电流，频率$\omega_0=\frac{2eV}{\hbar}$. 当存在频率为$\omega_1$的交变电磁场时，电磁场会对约瑟夫森结的交变电流产生调制. 当约瑟夫森结固有频率ω_0为ω_1的整数倍时，外加射频信号会与约瑟夫森结电流本身的振荡产生类似“共振”现象. 此时，电

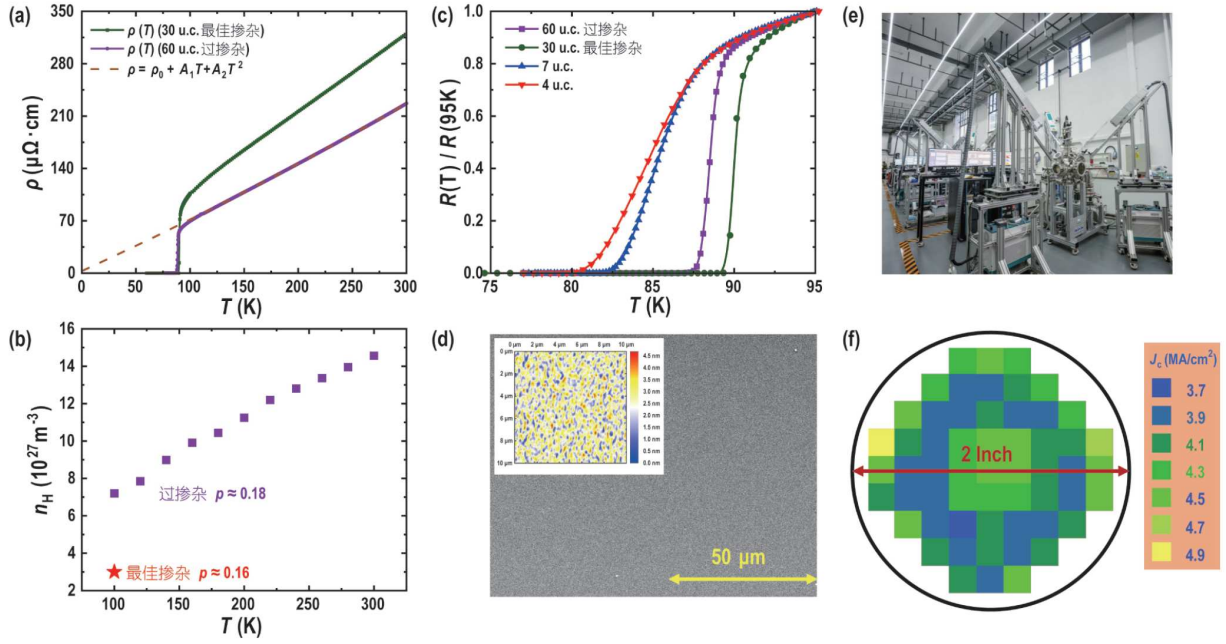


图 4 联合团队制备YBCO薄膜进展. (a) 60晶胞厚YBCO膜电阻率-温度曲线; (b) 霍尔载流子浓度; (c) 薄膜T_c的厚度依赖性; (d) 扫描电子显微镜图像与原子力显微镜图像; (e) 三光束脉冲激光共沉积系统; (f) 临界电流密度

Figure 4 Progress in the preparation of YBCO thin films by the joint team of the Institute of Physics, Chinese Academy of Sciences and the Songshan Lake Materials Laboratory. (a) Resistivity-temperature curve of a 60 unit cell thick YBCO film; (b) Hall carrier concentration; (c) superconducting transition temperature versus thicknesses; (d) scanning electron microscope image and atomic force microscope image; (e) three-beam pulsed laser co-deposition system; (f) critical current density

流-电压特性曲线会出现平坦的台阶, 即Shapiro台阶. 基于交流约瑟夫森效应和Shapiro台阶, 约瑟夫森结可用于直流—交流信号转化、信号探测以及电压基准等领域.

当平行于约瑟夫森结平面的磁通Φ通过结时, 超流的相位会在结内形成空间梯度, 导致临界电流出现Fraunhofer干涉图样. 对于1个矩形结, 有

$$I_c(\Phi) = I_{c0}\left|\frac{\sin\left(\frac{\pi\Phi}{\Phi_0}\right)}{\frac{\pi\Phi}{\Phi_0}}\right|, \tag{3}$$

其中, Φ_0为磁通量子. 在闭合超导回路中存在两个约瑟夫森结时, 通过回路的磁通Φ_{ex}会对两个约瑟夫森结之间的相位差形成调制:

$$\phi_1 - \phi_2 = \frac{2\pi\Phi_{ex}}{\Phi_0} + 2\pi n. \tag{4}$$

忽略环路自感的情况下, 超导回路的总电流为

$$I = 2I_c\cos\left(\frac{\pi\Phi_{ex}}{\Phi_0}\right)\sin\left(\frac{\phi_1+\phi_2}{2}\right). \tag{5}$$

通过调整偏置电流使得正弦项为1时, 得到环路最大临界电流:

$$I_{Max} = 2I_c\left|\cos\left(\frac{\pi\Phi_{ex}}{\Phi_0}\right)\right|. \tag{6}$$

利用这一特性, 可将约瑟夫森结制成超导量子干涉器件(superconducting quantum interference device, SQUID), 用于探测微弱磁场.

约瑟夫森结中不仅包含超导电流, 也可包含正常电流及位移电流, 可用电阻R_n和电容C并联的约瑟夫森结(resistively and capacitively shunted junction model, RCSJ)模型描述:

$$C\frac{dV}{dt} + \frac{V}{R_n} + I_c\sin\varphi = I. \tag{7}$$

隧穿约瑟夫森结一般有较大的电容, 在电流-电压曲线上存在回滞现象, 这对约瑟夫森结的应用不利. 而弱连接结构(势垒区为非绝缘体)的约瑟夫森结容易实现小电容值, 满足单值响应的需求.

弱连接约瑟夫森结的I_c与R_n和两端超导材料本身以及弱连接的材料种类、势垒区尺度有关. 当势垒区尺度L小于弱连接区域相干长度ξ时, 约瑟夫森结保持理想特性[68]: 电流与相位为正弦关系, 约瑟夫森结特征电压$V_c = I_cR_n$仅与超导材料本身有关. 当势垒尺度远大

于相干长度时，电流与相位不仅会脱离正弦函数依赖，还将出现多值关系，随势垒尺度的增大指数衰减，V_c随着势垒尺度增大而下降．所以对于弱连接结构的约瑟夫森结，需尽量缩小势垒层尺度．相较于传统超导材料制备的约瑟夫森结，高温超导材料由于极短的相干长度、复杂的化学和结构特性、对氧含量十分敏感等特点，给约瑟夫森结的制备带来了极大的挑战．

2.2 约瑟夫森结器件应用

基于约瑟夫森结的高温超导电子学器件将量子极限灵敏度与相对较高的工作温区相结合，既保持超导电子学器件的极致性能，又兼顾宜用性，在雷达通信、生物医学、地球物探、精密测量等前沿领域极具应用潜力．近年来，随着YBCO薄膜制备技术的不断进步，高温超导约瑟夫森结及阵列的性能、规模、均匀性和可重复性获得大幅提升，高温超导电子学器件的灵敏度、适用频段及工作温度等关键指标持续刷新纪录．下面简要介绍几种典型器件的研究/应用进展．

2.2.1 高温超导量子干涉器件

超导量子干涉器件由一个或两个约瑟夫森结与超导环路构成，基于约瑟夫森效应及磁通量子化原理，能够实现对磁通与磁场的高精度探测，极限探测精度[69]可小于10^{-15} T/$\sqrt{\text{Hz}}$，在生物医学、地质勘探、工业检测等领域具有重要应用价值，具体可参阅文献[70]．本文仅简述高温SQUID应用方面的最新进展．在生物医学领域，与低温超导脑磁图仪相比，基于高温SQUID的脑磁仪无需液氦制冷，其探测器可直接贴近患者头皮，从而增强探测信号．瑞典查尔莫斯大学Pfeiffer等人[71]和Andersen等人[72]开发的7通道高温超导脑磁图仪能检测到低温超导脑磁图仪无法识别的早期神经信号．在地质探测领域，相比于低温超导系统，高温超导地磁勘探系统具有重量轻、结构紧凑、便携性好等优势[73~75]．2019年，中国地质科学院地球物理地球化学勘察研究所开发的高温SQUID磁强计在辽宁省白云金矿床实现了最大深度达2500米的地质勘探[76]．在工业检测领域，高温SQUID凭借其探测微弱磁场的超高灵敏度已广泛应用于航空航天、能源、电力、核工业等多个领域的无损检测[77,78]．

SQUID的电压-磁通量($V-\Phi$)响应曲线具有周期性(周期为一个磁通量子Φ_0)，使其只能测量在一个磁通量子周期内的微小变化，通常无法直接测量磁场的绝对值，需要使用反馈电路锁定其工作点．将多个具有不同环路尺寸的SQUID串联或并联可构成超导量子干涉滤波器(superconducting quantum interference filter, SQIF)．SQIF的电压-磁场($V-H$)响应曲线呈现非周期性的单峰特性，可实现单值、线性范围显著提升的磁场-电压响应．高重复率、高可控性的高温超导约瑟夫森结阵列制备工艺是实现高性能SQIF器件的基础．2003~2006年间，德国耶拿大学研究组率先采用双晶结技术制备了串联、并联及串并联混合型高温SQIF磁强计，磁场噪声达到了当时高温超导磁强计探测绝对磁场的最高水平，SQIF中约瑟夫森结数量最多达到224个，磁场电压转换灵敏度最高达8400 V/T[79~82]．2008年，美国加州大学伯克利分校Cybart等人开始用离子辐照损伤技术制作SQIF[83]，之后，法国巴黎-萨克雷大学[84~86]用氧离子辐照研制了最多4000个结的SQIF阵列，其灵敏度最高超过1000 V/T．澳大利亚研究组Mitchell等人[87,88]基于台阶结技术制备了包含多达20000个YBCO约瑟夫森结的SQIF器件，灵敏度达到1530 V/T．SQIF器件性能与SQUID阵列单元的数量和约瑟夫森结参数(尤其是临界电流I_c)的均匀性密切相关[89]．2022年，Cybart研究组首次用聚焦氦离子束技术研制高集成度的高温SQIF阵列[90]．高温SQIF阵列的发展趋势如图5(a), (b)，及表S1所示．

2.2.2 高温超导太赫兹混频器

高温超导太赫兹混频器利用约瑟夫森结的非线性伏安特性实现微波/太赫兹信号的频率转换．图5(c)为高温超导太赫兹混频器、低温超导混频器(包括热电子混频器、隧道结混频器)和半导体混频器的噪声温度和工作频率的对比，更多的性能参数可见补充表S2．在太赫兹频段，超导混频器具有比半导体混频器更低的噪声温度，且对本振信号的功率需求比半导体器件低3个数量级以上，更适宜于多通道阵列化应用．在超导混频器中，隧道结混频器的噪声温度接近量子极限，但其工作频率上限受超导能隙的限制；在1 THz及以上频率，主要采用热电子混频器，但其中频带宽较低．相比之下，高温超导混频器兼具噪声低、带宽大和制冷系统轻巧的综合优势，可以提高现有空天基太赫兹通信、探测和成像系统的信号接收灵敏度，在重量/体积/功耗等资源受限的平台中有广阔的应用前景．关于高温超导太赫兹混频器的更多内容可参阅文献[91]．

高温超导混频器的噪声温度、转换增益(输出中频信号功率与输入射频信号功率之比)等关键参数主要

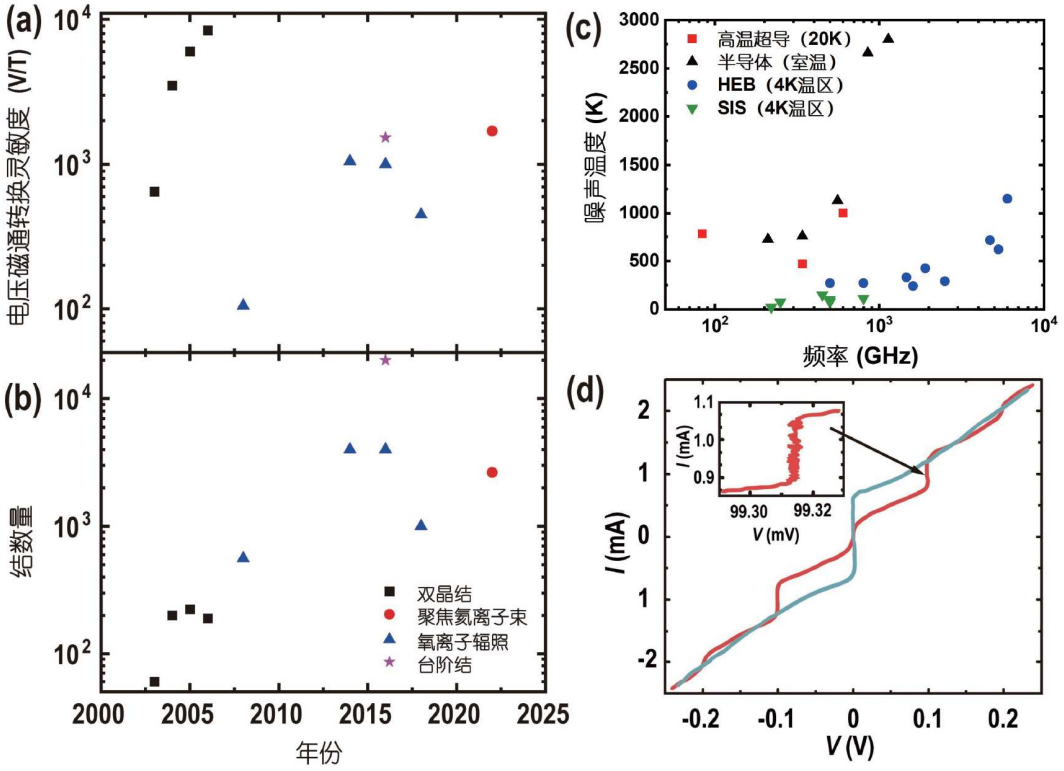


图 5 (a) 2003年以来[79~88,90]不同技术的高温SQIF所测得的磁场电压转换灵敏度; (b) 高温SQIF阵列中集成的约瑟夫森结数量的变化趋势; (c) 高温超导约瑟夫森结混频器和半导体混频器、低温超导混频器(包括热电子探测器(hot electron bolometer, HEB)混频器和超导体-绝缘体-超导体(superconductor-insulator-superconductor, SIS)混频器)的噪声温度和工作频段的对比[92,95~110]; (d) 620个YBCO约瑟夫森结在77.465 GHz, 79.2 K下的*I-V*曲线, 电压台阶的宽度约为0.1 V[94]

Figure 5 (a) Magnetic field-to-voltage transfer sensitivity of high-temperature SQIFs using different technologies since 2003[79-88,90]; (b) evolution of the number of integrated Josephson junctions in high-temperature SQIF arrays; (c) comparison of noise temperature and operational frequency bands among HTS Josephson junction mixers, semiconductor mixers, and low-temperature superconducting mixers (including hot electron bolometer (HEB) mixers and superconductor-insulator-superconductor (SIS) mixers)[92,95–110]; (d) current-voltage (*I-V*) curves of 620 YBCO Josephson junctions at 77.465 GHz and 79.2 K, with a voltage step width of approximately 0.1 V[94]

依赖于约瑟夫森结的特征参数. 高R_n有助于改善约瑟夫森结与前后级电路的匹配, 进而提高混频器的转换增益, 而高V_c有助于降低噪声温度. 北京理工大学高翔等人[92]与澳大利亚联邦科学与工业研究组织合作利用YBCO台阶结研制出340 GHz混频器, 通过优化天线结构和约瑟夫森结参数, 在20 K实现了1.5 dB的正转换增益和470 K的噪声温度(对应约瑟夫森结$R_n\approx5.7\Omega$, $I_cR_n\approx2.7$ mV), 而40 K转换增益和噪声温度分别为–1 dB和780 K(对应约瑟夫森结$R_n>5\Omega$, $I_cR_n\approx2$ mV), 所需本振功率仅–40 dBm(0.1 μW), 为当前高温超导太赫兹混频器公开报道的最佳值, 也远优于同频段半导体混频器.

2.2.3 电压基准

交流约瑟夫森效应将电压与频率关联, 具有极高的精度和可复现性, 是目前国际公认的电压基准的物理基础. 低温超导电压基准工作于液氦温区, 制冷代价大, 限制了其应用场景和工业推广. 而高温超导电压基准可工作于液氮温区, 将显著降低运行成本并提升系统的便携性. 美国、日本、俄罗斯及欧洲多国计量机构已积极投入高温超导电压基准的研发[93]. 德国联邦物理技术研究院Klushin等人[94]研制的高温超导电压基准芯片(620个双晶结串联)可实现0.1 V电压的稳定输出, 如图5(d)所示. 电压基准应用要求约瑟夫森结阵列中的所有结在微波辐照下的响应必须同步. 为了实现伏特级的电压输出, 结阵列规模需达到千级乃至万级, 因此亟需大规模、高均匀性、可重复性的高温超导约瑟夫森结阵列制备技术.

2.3 约瑟夫森结制备

早期高温超导约瑟夫森结主要有双晶结、台阶

结、台阶SNS结以及斜边结等几种制备方式. 此外, 人们还尝试使用离子束辐照的方式制备高温超导约瑟夫森结[111], 但是由于辐照区域较宽, 约瑟夫森结性能并不理想. 由于聚焦He离子束(focused helium ion beam, He-FIB)具有极小的聚焦半径(约0.5 nm), 利用He-FIB制备高温超导约瑟夫森结逐渐被国内外研究组采用, 约瑟夫森结的关键参数也逐步接近台阶结和双晶结的水平. 这项技术有望帮助人们获得稳定可靠、可实现批量化生产的高温超导约瑟夫森结器件.

2.3.1 双晶结

双晶结是一种基于双晶衬底(bicrystal substrate)构建的高温超导弱连接结构.其制备过程首先涉及将两块单晶衬底(如$SrTiO_3$、MgO等)在特定晶向角(θ, 例如24°、30°)下进行晶向融合, 形成双晶衬底, 如图6(a)所示. 随后, 在该双晶衬底上外延生长高温超导薄膜. 由于薄膜的晶格取向继承自衬底, 因此在衬底晶界(grain boundary, GB)处自然形成相应的晶界弱连接, 即双晶结[112]. 该晶界区域由于晶格失配、氧空位聚集以及超导序参量(superconducting order parameter)被抑制, 形成一个纳米尺度(厚度1~2 nm)的势垒.

双晶结的一个显著特点是其晶界取向角θ可被精确调控, 通过系统性地改变θ值, 能够有效调节结的关键特性(如临界电流密度J_c). 双晶结的临界电流密度与晶界角存在指数衰减关系, 即$J_c \sim J_0\exp(-\frac{\theta}{\theta_0})$, 其中$J_0$为YBCO薄膜的临界电流密度. 同时, 结电阻随着晶界角增大而增大. 曾有文献报道I_cR_n与J_c存在$I_cR_N \sim J_c^{0.5}$的关系[113].

早期的双晶结采用面内倾斜结构, 其77 K下的V_c一般在0.1~0.3 mV. 而采用基底面倾斜双晶结(bi-epitaxial tilt junction, BTJ)结构, 可显著提升双晶结的V_c. Poppe等人[114]通过衬底处理等手段, 在12°对称倾斜的衬底上生长YBCO双晶结(晶界角度为24°), 77 K下的V_c最高可达1.2 mV. 在结阵列制备方面, 如前所述, Klushin等人[94]利用双晶结制备了具有620个YBCO约瑟夫森结的阵列, 用于量子基准电压输出.

2.3.2 台阶结

台阶结(step-edge junction)是一种通过刻蚀技术在单晶衬底(如MgO)特定位置制备出缓坡台阶, 随后外延生长YBCO薄膜所形成的弱连接结构[115]. 由于薄膜在台阶斜坡区域与平面区域的生长取向存在差异, 从而形成了一种晶界型约瑟夫森结, 如图6(b)所示.

台阶结的约瑟夫森临界电流、结电阻等参数不仅与台阶的高度和角度有关[116], 台阶的微观结构(如粗糙度和陡峭度)也会显著影响台阶结的性能. 十余年来, 持续优化MgO衬底上的台阶显著提升了台阶结的性能[117~120]. Kaczmarek等人[118]提出了一种创新性的双层

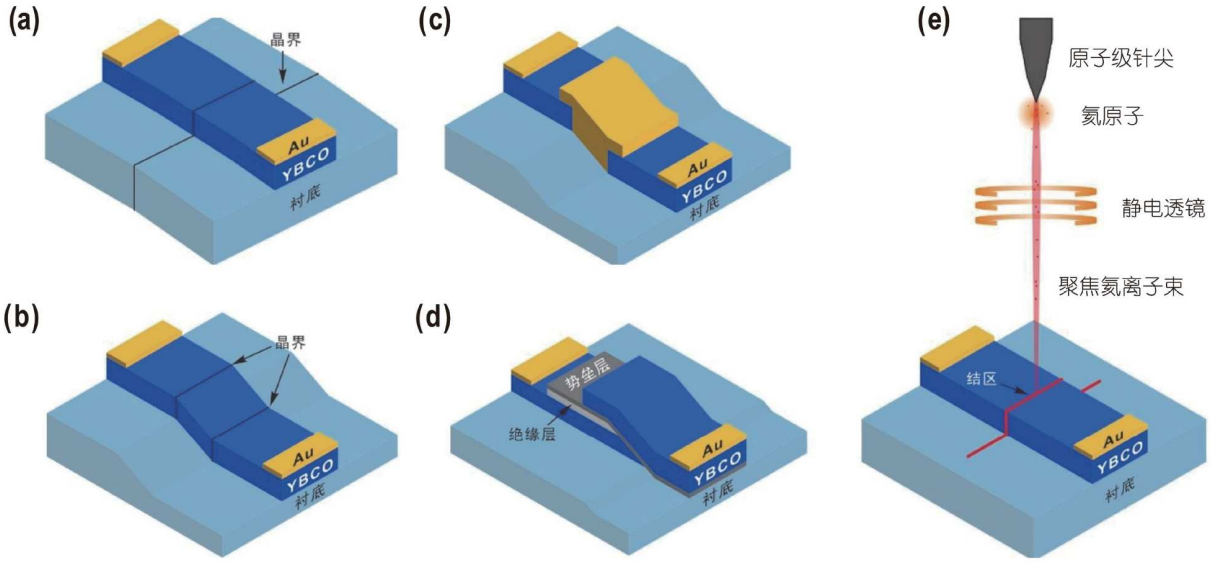


图 6 主流的高温超导约瑟夫森结制备技术. (a) 双晶结; (b) 台阶结; (c) 台阶SNS结; (d) 斜边结; (e) He-FIB结

Figure 6 Main preparation techniques for high-temperature superconducting Josephson junctions. (a) Bi-crystal junction; (b) step-edge junction; (c) step SNS junction; (d) inclined edge junction; (e) He-FIB junction

缓冲结构: 首先沉积约10 nm厚的非超导YBCO薄膜作为“种子层”, 再覆盖约30 nm厚的$SrTiO_3$“阻挡层”. 利用该结构, 他们在MgO衬底的45°台阶上成功制备了高质量YBCO薄膜, 其T_c约93 K, 在77 K下的临界电流密度J_c约5 MA/cm^2, V_c最高可达0.7 mV左右, 其制备的DC SQUID在白噪声频段的磁场灵敏度达到20 fT/Hz$^{1/2}$.

相较于双晶结, 台阶结可通过调整刻蚀台阶的位置来选择约瑟夫森结的位置, 因而在结阵列器件的制备方面具有较大优势. 2016年, Mitchell等人[87]利用台阶结技术, 成功制备了包含多达20000个YBCO约瑟夫森结的SQIF器件, 这是目前单片集成高温超导约瑟夫森结数量的最高记录.

2.3.3 台阶SNS结

台阶SNS结是通过刻蚀手段, 在衬底上刻蚀出一个陡峭的台阶, 再在衬底上生长高温超导薄膜, 如图6(c)所示. 由于台阶处十分陡峭, 台阶边缘没有超导薄膜沉积. 随后, 在超导薄膜上沉积一层金属, 一般是Au或者Ag, 从而形成SNS结. 台阶SNS结在77 K时的I_cR_n最高可到达1 mV[121]. 但是SNS结中往往存在较大比例的过剩电流, 且SNS结的R_n主要来源于超导薄膜与金属的界面电阻[122,123]. 界面电阻的存在给台阶SNS结的稳定性带来了很大的挑战, 同时也使约瑟夫森结临界电流分布变宽、一致性变差.

2.3.4 斜边结

斜边结的制备方法是先在衬底上生长高温超导薄膜以及一层绝缘材料薄膜, 随后利用离子束刻蚀或者湿法刻蚀10°~20°的平缓台阶, 最后再生长一层极薄的绝缘层(作为势垒层)和超导电极, 如图6(d)所示. 日本研究组采用$SrSnO_3$/La-$YBa_2Cu_3O_7$/$SrSnO_3$/La-YBa_2-Cu_3O_7多层结构, 利用界面控制工艺将1000个左右的约瑟夫森结临界电流的离散性降低至8%以内[124,125]. 斜边结由于顶电极的存在, 具有较好的稳定性和抗干扰能力.

2.3.5 聚焦He离子束技术

聚焦He离子束(He-FIB)技术是超尖端灯丝原位成形技术的突破, 并结合气态场离子源技术进一步发展的结果[126]. 它利用低温冷却的钨灯丝作为阳极, 使其处于含有极少量He气的低真空氛围中, 再通过高压脉冲修饰钨丝, 使其尖端仅保留3个原子. 在正电场加速下, 三个原子会发射3束He离子束, 通过调整光阑孔对其中的一束He离子束进行聚焦, 如图6(e)所示. 由于He离子半径小, 且它的离子束仅仅来源于1个原子, 其束斑尺寸可达到0.5 nm量级. 因He离子质量远小于Ga离子, 对样品的损伤较小, 可用于加工10 nm以下的纳米孔洞器件[127].

2015年, Cybart等人[128]率先利用He-FIB技术, 通过改变He离子辐照剂量, 分别制备出了具有金属性势垒和绝缘性势垒的YBCO约瑟夫森结. 研究表明, He-FIB低剂量辐照, 并未使YBCO受到辐照的区域产生非晶化. Müller等人[129]利用透射电镜观察结区结构, 在形成约瑟夫森结的剂量范围内, 辐照区域并未发生结构变化. 当辐照大于1500 ions/nm时, 可以观察到非晶化区域, 其宽度随着剂量增加而线性增大. 在低剂量下, He离子束对YBCO的作用主要是造成氧原子缺失, 使得受辐照区域逐渐向Mott绝缘体转变. Karrer等人[130]测量了He-FIB制备的YBCO约瑟夫森结性能随时间的演化. 在300天内重复测量发现, 储存在室温氮气环境下器件的临界电流密度J_c随时间增加, 并且满足$J_c \propto e^{(-\sqrt{t/\tau})}$的扩散模型. 这说明随着时间推移, 部分氧原子会重新扩散回原位, 并且弛豫时间τ随着He离子剂量的提高而增加. 而在氧气氛围中退火, 器件在一周内可进入稳定状态.

Cho等人[131]和Li等人[132]利用He-FIB制备的SQUID器件, 其低频磁通噪声水平达到20 $\mu\Phi_0$/Hz$^{1/2}$ (μ=10^{-6}), 其最小环路尺寸达到10 nm. 美国加州大学研究组与Quantum Design公司合作将聚焦氦离子束制备的高温SQUID集成在综合多物性测量系统(physical properties measurement systems, PPMS)中, 实现了宽温区(1~50 K)、噪声约100 pT/Hz$^{1/2}$@50 K的高温SQUID磁测量系统[133]. 除此之外, 该课题组还利用He-FIB技术加工了诸如量子比特、THz混频器、高温超导逻辑电路等实用化高温超导器件[134~136].

相较于其他技术手段, 聚焦He离子束是在器件完成图形化后开始约瑟夫森结的制备, 且可在器件的任意位置进行约瑟夫森结加工. He离子束斑的纳米量级尺寸保障了极高的加工精度和自由度. 基于以上特点, He-FIB可以实现高密度的结阵列加工, 约瑟夫森结之间的间隙可小于100 nm. 例如, 加州大学在5 mm×5 mm的YBCO薄膜上集成了2640个结的超导干涉滤波器(SQIF)[90]芯片, 磁场探测灵敏度可达1700 V/T. Schmid等人[137]利用He-FIB技术, 制备了结区面积仅为1 μm^{2}的YBCO约瑟夫森结二极管器件, 其临界电流的各向异性比达到7, 是目前约瑟夫森结二极管器件的最好结果, 在电路集成化方面有巨大优势, 在非互易超导电子学和超导逻辑器件方面具有潜在应用价值. 此外, He-FIB还可

实现纳米尺度的高温超导器件加工, 例如纳米尺度SQUID[138]及其阵列[139]、高温超导纳米线[140,141]等, 可应用于扫描SQUID探针以及单光子探测等领域.

He-FIB技术被用于高温超导约瑟夫森结制备后, 迅速受到国内外研究组的关注. 北京大学、中国科学院微系统研究所和物理研究所等研究团队都利用He-FIB在YBCO上成功制备了约瑟夫森结器件. 其中, 北京大学不仅将这项技术运用在YBCO上, 还成功在MgB_2以及铁基超导材料上制备了约瑟夫森结[142~146].

中国科学院物理研究所团队制备了高质量的YBCO薄膜(图4), 优化微纳加工工艺, 使He-FIB约瑟夫森结的单结性能和结阵列集成度达到国际先进水平. 约瑟夫森单结在77 K的特征电压最高达到0.42 mV, 而2000个约瑟夫森结阵列能够在0.5 mm×0.5 mm范围内实现集成, 如图7(a), (b)和(f)所示. 其中, 单个测量通道内串联了50个约瑟夫森结, 结间距为200 nm, 如图7(c)所示, Shapiro台阶宽度为单结的50倍, 说明约瑟夫森结阵列具有良好的均匀性和相位相干性, 如图7(e)所示. 结合上述结果, 不同约瑟夫森结制备技术的单结参数与结阵列数量总结于表2.

为进一步提升He-FIB约瑟夫森结的性能和一致性, 首先要持续提高薄膜质量, 其次需要抑制He离子与YBCO薄膜作用过程中的横向散射, 增强束流准直性, 最后需建立He-FIB约瑟夫森结微观结构与物性的构效关系, 为工艺的进一步优化提供指导.

3 总结与展望

在高温超导机理方面, YBCO薄膜与约瑟夫森结已为超导参量演化、电子结构、能隙对称性等研究方向提供了重要线索. 在高温超导应用方面, 从YBCO薄膜

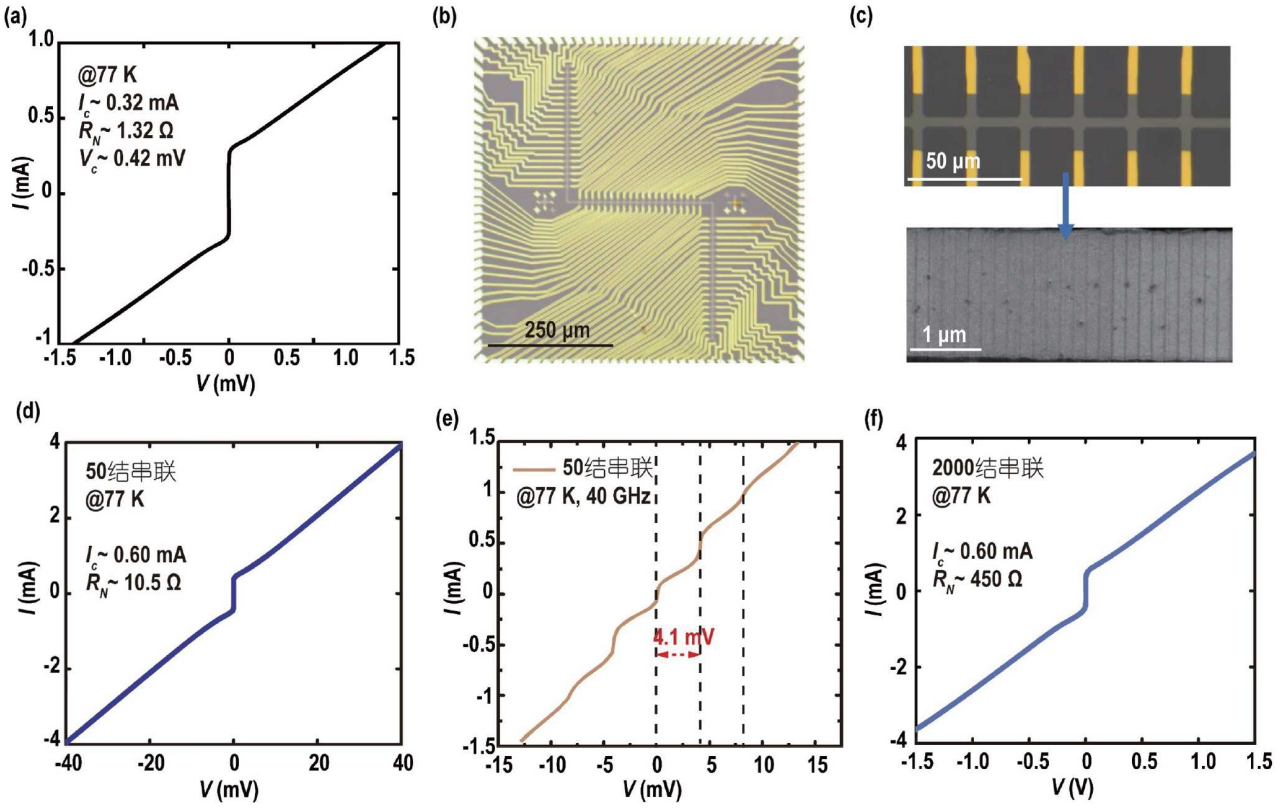


图 7 中国科学院团队制备的约瑟夫森结与结阵列器件. (a) 77 K时, He-FIB结特征电压最高可达~0.42 mV; (b) 2000结串联芯片; (c) 放大的约瑟夫森结桥路SEM图像; (d) 2000结集成芯片中的单通道50结串联的电流-电压曲线(77 K); (e) 单通道(50结)串联Shapiro台阶; (f) 2000结串联电流-电压曲线(77 K)

Figure 7 Josephson junctions and junction array devices prepared by the team of the Chinese Academy of Sciences. (a) At 77 K, the current characteristic voltage of the current feature of the He-FIB junction can reach approximately 0.42 mV at present; (b) 2000 junction series chip; (c) SEM image of the enlarged Josephson junction bridge circuit; (d) the current-voltage curve of a single-channel 50 junction series in the 2000 junction integrated chip (77 K); (e) single-channel (50 junction) series Shapiro step; (f) the current-voltage curve of the 2000 junction series (77 K)

表 2 主流YBCO约瑟夫森结制备技术的单结参数与结阵列数量[87,90,94,125,147~150]a)

Table 2 Single-junction parameters and the numbers of junction arrays of common YBCO Josephson junction fabrication techniques[87,90,94,125,147–150]

技术路线		双晶结	台阶结	台阶SNS结	斜边结	He-FIB结
技术特点	V_c (μV)@77 K	100~1200	100~700	10~1000	12~400	400以内
	自由度	低	中等	中等	中等	高
约瑟夫森结数量	国内	2	2	n/a	n/a	2000
	国外	~600	~20000	n/a	~1000	~2640

a) n/a表示缺少准确数据

生长, 到约瑟夫森结制备, 再到阵列化、集成化器件的完整链条已被实现. 历经近40年的技术迭代和经验累积, YBCO薄膜和约瑟夫森结的性能已大幅提高, 产生了一定社会价值和经济价值.

YBCO薄膜已取得以下进展: (1) 在最佳掺杂实现T_c>90 K; (2) 覆盖p=0.18及以下的所有Cu-O链掺杂水平; (3) 表面颗粒物<5个/(100 μm)^2; (4) 实现大面积均匀的T_c~88 K和J_c~3 MA/cm^2@77 K; (5) 通过界面提升YBCO薄膜的T_c和调制电子结构(如线性电阻率、电荷密度波与赝能隙等). 尚有如下问题有待解决: (1) 薄膜T_c低于单晶T_c; (2) 最佳掺杂薄膜的相位刚度仅为单晶的1/4左右; (3) 薄膜的微波表面电阻的下限(目前R_s(77 K, 10 GHz)=0.18 mΩ); (4) 薄膜表面存在数纳米的高低起伏, 影响约瑟夫森结加工稳定性; (5) Cu-O链氧含量均匀性和去孪晶化未完全实现. 发展更系统性的界面控制, 包括衬底截止面处理、缓冲层、保护层、异质结与超晶格结构, 辅以活性氧源退火技术, 是解决上述问题的重要思路.

YBCO约瑟夫森结的制备技术从经验调控走向精准设计, He-FIB与台阶结技术更展示出其在阵列化方面的巨大优势. YBCO约瑟夫森结的临界电流I_c、结电阻R_n、特征电压V_c=I_cR_n等关键参数不断优化, 约瑟夫森结阵列的规模、一致性与可控性显著提升, 为高温超导电子器件的实用化奠定了坚实基础. 目前YBCO约瑟夫森结仍面临以下挑战: (1) 大规模约瑟夫森结阵列中, 临界电流I_c、结电阻R_n、特征电压V_c=I_cR_n分布仍存在8%左右的波动, 影响器件整体性能; (2) 结区氧含量发生时间弛豫、界面退化等现象, 制约器件的长期可靠运行. 未来, YBCO约瑟夫森结技术的发展应聚焦于以下方向: (1) 优化纳米加工技术, 如提升He-FIB束流准直性、减少横向损伤, 从而实现更高精度、更高一致性的结阵列制备; (2) 发展原位退火技术, 调制结区氧含量, 改善约瑟夫森结性能; (3) 建立约瑟夫森结微观结构与物性的构效关系, 指导工艺优化.

通过薄膜生长与约瑟夫森结制备技术的协同创新, YBCO约瑟夫森结有望在量子传感、太赫兹通信、电压基准等战略领域中实现规模化应用, 推动高温超导电子学从实验室走向产业化.

致谢 感谢中国科学院物理研究所陈其宏、李洋沐、杨立红、林泽丰、胡卫, 中国科学院上海微系统与信息技术研究所李浩, 宁波大学孔祥燕, 南开大学何明在本文写作和绘图中提供的有益讨论.

参考文献

1 Zhao Z X, Chen L Q, Yang Q X et al. Superconductivity in the liquid nitrogen temperature rangeof Ba-Y-Cu oxide (in Chinese). Chin Sci Bull, 1987, 32: 412–414 [赵忠贤, 陈立泉, 杨乾声, 等. Ba-Y-Cu氧化物液氮温区的超导电性. 科学通报, 1987, 32: 412–414]

2 Wu M K, Ashburn J R, Torng C J, et al. Superconductivity at 93 K in a new mixed-phase Y-Ba-Cu-O compound system at ambient pressure. Phys Rev Lett, 1987, 58: 908–910

3 Liang R, Dosanjh P, Bonn D A, et al. Growth and properties of superconducting YBCO single crystals. Physica C-Supercond, 1992, 195: 51–58

4 Edwards H L, Markert J T, de Lozanne A L. Energy gap and surface structure of $YBa_2Cu_3O_{7-x}$ probed by scanning tunneling microscopy. Phys Rev Lett, 1992, 69: 2967–2970

5 Hosseini A, Harris R, Kamal S, et al. Microwave spectroscopy of thermally excited quasiparticles in $YBa_2Cu_3O_{6.99}$. Phys Rev B, 1999, 60: 1349–1359

6 Smith J A, Cima M J, Sonnenberg N. High critical current density thick MOD-derived YBCO films. IEEE Trans Appl Supercond, 2002, 9: 1531–

1534
7 Terashima T, Shimura K, Bando Y, et al. Superconductivity of one-unit-cell thick $YBa_2Cu_3O_7$ thin film. Phys Rev Lett, 1991, 67: 1362–1365
8 Matsuda Y, Komiyama S, Onogi T, et al. Thickness dependence of the Kosterlitz-Thouless transition in ultrathin $YBa_2Cu_3O_{7-\delta}$ films. Phys Rev B, 1993, 48: 10498–10503
9 Savvides N, Katsaros A. Growth and evolution of microstructure of epitaxial $YBa_2Cu_3O_{7-x}$ ultrathin and thin films on MgO. Physica C-Supercond, 1994, 226: 23–36
10 Sekitani T, Miura N, Ikeda S, et al. Upper critical field for optimally-doped $YBa_2Cu_3O_{7-\delta}$. Physica B-Condensed Matter, 2004, 346-347: 319–324
11 Sekitani T, Matsuda Y H, Miura N. Measurement of the upper critical field of optimally-doped $YBa_2Cu_3O_{7-\delta}$ in megagauss magnetic fields. New J Phys, 2007, 9: 47
12 Zuev Y, Seog Kim M, Lemberger T R. Correlation between superfluid density and T_C of underdoped $YBa_2Cu_3O_{6+x}$ near the superconductor-insulator transition. Phys Rev Lett, 2005, 95: 137002
13 Hetel I, Lemberger T R, Randeria M. Quantum critical behaviour in the superfluid density of strongly underdoped ultrathin copper oxide films. Nat Phys, 2007, 3: 700–702
14 Stangl A, Palau A, Deutscher G, et al. Ultra-high critical current densities of superconducting $YBa_2Cu_3O_{7-\delta}$ thin films in the overdoped state. Sci Rep, 2021, 11: 8176
15 Antončík F, Jankovský O, Hlásek T, et al. Nanosized pinning centers in the rare earth-barium-copper-oxide thin-film superconductors. Nanomaterials, 2020, 10: 1429
16 Talantsev E F, Strickland N M, Wimbush S C, et al. Hole doping dependence of critical current density in $YBa_2Cu_3O_{7-\delta}$ conductors. Appl Phys Lett, 2014, 104: 242601
17 Llordés A, Palau A, Gázquez J, et al. Nanoscale strain-induced pair suppression as a vortex-pinning mechanism in high-temperature superconductors. Nat Mater, 2012, 11: 329–336
18 Xiong P Y, Chen F C, Feng Z P, et al. Optimization of large-area $YBa_2Cu_3O_{7-\delta}$ thin films by pulsed laser deposition for planar microwave devices. Chin Phys B, 2023, 32: 077402
19 Takanashi N, Kondo M, Matsui H, et al. Effect of introduction of artificial pinning center in $YBa_2Cu_3O_y$ thin films to reduce surface resistancece. IEEE Trans Appl Supercond, 2017, 27: 1–4
20 Honma T, Sato S, Sato K, et al. Microwave surface resistance of YBCO superconducting thin films under high DC magnetic field. Physica C-Supercond, 2013, 484: 46–48
21 Sato S, Honma T, Takahashi S, et al. Introducing artificial pinning centers into YBCO thin films to improve surface resistance in a DC magnetic field. IEEE Trans Appl Supercond, 2012, 23: 7200404
22 Wahlberg E, Arpaia R, Seibold G, et al. Restored strange metal phase through suppression of charge density waves in underdoped $YBa_2Cu_3O_{7-\delta}$. Science, 2021, 373: 1506–1510
23 Solovjov A L, Omelchenko L V, Stepanov V B, et al. Specific temperature dependence of pseudogap in $YBa_2Cu_3O_{7-\delta}$ nanolayers. Phys Rev B, 2016, 94: 224505
24 Hamet J F, Mercey B, Hervieu M, et al. *a*-Axis oriented superconductive YBCO thin films. Physica C-Supercond, 1992, 198: 293–302
25 Dekkers J M, Rijnders G, Harkema S, et al. Monocrystalline $YBa_2Cu_3O_{7-x}$ thin films on vicinal $SrTiO_3$ (001) substrates. Appl Phys Lett, 2003, 83: 5199–5201
26 Arpaia R, Andersson E, Kalaboukhov A, et al. Untwinned $YBa_2Cu_3O_{7-\delta}$ thin films on MgO substrates: a platform to study strain effects on the local orders in cuprates. Phys Rev Mater, 2019, 3: 114804
27 He Q, Peng E, Zhang J, et al. Synchrotron 3D-RSM reveals the microstructure of superconducting $YBa_2Cu_3O_{7-x}$ films grown on various substrates. Appl Phys Lett, 2025, 126: 124102
28 Tsuei C C, Kirtley J R. Pairing symmetry in cuprate superconductors. Rev Mod Phys, 2000, 72: 969–1016
29 Grissonnanche G, Cyr-Choinière O, Laliberté F, et al. Direct measurement of the upper critical field in cuprate superconductors. Nat Commun, 2014, 5: 3280
30 Liang R, Dosanjh P, Bonn D A, et al. Lower critical fields in an ellipsoid-shaped $YBa_2Cu_3O_{6.95}$ single crystal. Phys Rev B, 1994, 50: 4212–4215
31 Ando Y, Segawa K. Magnetoresistance of untwinned $YBa_2Cu_3O_y$ single crystals in a wide range of doping: anomalous hole-doping dependence of the coherence length. Phys Rev Lett, 2002, 88: 167005
32 Basov D N, Liang R, Bonn D A, et al. In-plane anisotropy of the penetration depth in $YBa_2Cu_3O_{7-x}$ and $YBa_2Cu_4O_8$ superconductors. Phys Rev Lett, 1995, 74: 598–601
33 Homes C C, Timusk T, Bonn D A, et al. Optical properties along the *c*-axis of $YBa_2Cu_3O_{6+x}$, for $x = 0.50 \rightarrow 0.95$ evolution of the pseudogap. Physica C-Supercond, 1995, 254: 265–280
34 Lin Z F, Sun W X, Liu T X, et al. Research progress on superconducting films prepared by pulsed laser deposition (in Chinese). J Synth Cryst,

2023, 52: 1036–1051 [林泽丰, 孙伟轩, 刘天想, 等. 脉冲激光沉积技术制备超导薄膜的研究进展. 人工晶体学报, 2023, 52: 1036–1051]
35 Westerheim A C, Yu-Jahnes L S, Anderson A C. Off-axis magnetron sputtering of YBCO films: the influence of atomic oxygen. IEEE Trans Magn, 1991, 27: 1001–1005
36 Lesueur J, Aprili M, Horton T J, et al. Properties of thin and ultra-thin YBCO films grown by a Co-evaporation technique. J Alloys Compd, 1997, 251: 156–160
37 Hirai T, Yamane H. MOCVD superconducting oxide films. J Cryst Growth, 1991, 107: 683–691
38 Puig T, Gutierrez J, Obradors X. Impact of high growth rates on the microstructure and vortex pinning of high-temperature superconducting coated conductors. Nat Rev Phys, 2024, 6: 132–148
39 Hammond R H, Bormann R. Correlation between the *in situ* growth conditions of YBCO thin films and the thermodynamic stability criteria. Physica C-Supercond its Appl, 1989, 162-164: 703–704
40 Liang R, Bonn D A, Hardy W N. Evaluation of CuO_2 plane hole doping in $YBa_2Cu_3O_{6+x}$ single crystals. Phys Rev B, 2006, 73: 180505
41 Berkley D D, Goldman A M, Johnson B R, et al. Techniques for the growth of superconducting oxide thin films using pure ozone vapor. Rev Sci Instruments, 1989, 60: 3769–3774
42 Endo T, Itoh K, Horie M, et al. Low-temperature process and growth enhancement of a-oriented $YBa_2Cu_3O_x$ thin films by oxygen plasmama. Physica C-Supercond, 2000, 333: 181–186
43 Yuan J, Chen Q, Jiang K, et al. Scaling of the strange-metal scattering in unconventional superconductors. Nature, 2022, 602: 431–436
44 Hücker M, Christensen N B, Holmes A T, et al. Competing charge, spin, and superconducting orders in underdoped $YBa_2Cu_3O_y$. Phys Rev B, 2014, 90: 054514
45 Badoux S, Tabis W, Laliberté F, et al. Change of carrier density at the pseudogap critical point of a cuprate superconductor. Nature, 2016, 531: 210–214
46 Ramshaw B J, Sebastian S E, McDonald R D, et al. Quasiparticle mass enhancement approaching optimal doping in a high-T_c superconductor. Science, 2015, 348: 317–320
47 Lyatti M, Savenko A, Poppe U. Ultra-thin $YBa_2Cu_3O_{7-x}$ films with high critical current density. Supercond Sci Technol, 2016, 29: 065017
48 Yu Y, Ma L, Cai P, et al. High-temperature superconductivity in monolayer $Bi_2Sr_2CaCu_2O_{8+\delta}$. Nature, 2019, 575: 156–163
49 Zhai H Y, Chu W K. Effect of interfacial strain on critical temperature of $YBa_2Cu_3O_{7-\delta}$ thin films. Appl Phys Lett, 2000, 76: 3469–3471
50 Biswas A, Yang C H, Ramesh R, et al. Atomically flat single terminated oxide substrate surfaces. Prog Surf Sci, 2017, 92: 117–141
51 Schlepütz C M, Björck M, Koller E, et al. Structure of ultrathin heteroepitaxial superconducting $YBa_2Cu_3O_{7-x}$ films. Phys Rev B, 2010, 81: 174520
52 Garcia-Barriocanal J, Perez-Muñoz A M, Sefrioui Z, et al. Disorder-controlled superconductivity at $YBa_2Cu_3O_7/SrTiO_3$ interfaces. Phys Rev B, 2013, 87: 245105
53 Fête A, Rossi L, Augieri A, et al. Ionic liquid gating of ultra-thin $YBa_2Cu_3O_{7-x}$ films. Appl Phys Lett, 2016, 109: 192601
54 Smilde H J H, Ariando H J H, Blank D H A, et al. *d*-Wave–induced Josephson current counterflow in $YBa_2Cu_3O_7$ / Nb zigzag junctions. Phys Rev Lett, 2002, 88: 057004
55 Kirtley J R, Tsuei C C, Ariando C C, et al. Angle-resolved phase-sensitive determination of the in-plane gap symmetry in $YBa_2Cu_3O_{7-\delta}$. Nat Phys, 2006, 2: 190–194
56 Gurvitch M, Fiory A T. Resistivity of $La_{1.825}Sr_{0.175}CuO_4$ and $YBa_2Cu_3O_7$ to 1100 K: absence of saturation and its implications. Phys Rev Lett, 1987, 59: 1337–1340
57 Wuyts B, Moshchalkov V V, Bruynseraede Y. Resistivity and Hall effect of metallic oxygen-deficient $YBa_2Cu_3O_x$ films in the normal state. Phys Rev B, 1996, 53: 9418–9432
58 Haage T, Zegenhagen J, Li J Q, et al. Transport properties and flux pinning by self-organization in $YBa_2Cu_3O_{7-\delta}$ films on vicinal $SrTiO_3$ (001). Phys Rev B, 1997, 56: 8404–8418
59 Yuan J, Shi L, Yue L, et al. Dynamical interplay between superconductivity and pseudogap in cuprates as revealed by terahertz third-harmonic generation spectroscopy. Sci Adv, 2024, 10: eadg9211
60 Li C G, Wang X, Wang J, et al. The high temperature superconducting filters and its application progress (in Chinese). Chin Sci Bull, 2017, 62: 4010–4024 [李春光, 王旭, 王佳, 等. 高温超导滤波器及其应用研究进展. 科学通报, 2017, 62: 4010–4024]
61 Face D W, Pellicone F M, Small R J, et al. $Tl_2Ba_2CaCu_2O_8$ and $YBa_2Cu_3O_7$ films on large area MgO and sapphire substrates for high power microwave and rf applications. IEEE Trans Appl Supercond, 1999, 9: 2492–2495
62 Face D W, Small R J, Warrington M S, et al. Large area $YBa_2Cu_3O_7$ and $Tl_2Ba_2CaCu_2O_8$ thin films for microwave and electronic applications. Physica C-Supercond, 2001, 357-360: 1488–1494
63 Einfeld J, Lahl P, Kutzner R, et al. Reduction of the microwave surface resistance in YBCO thin films by microscopic defects. Physica C-Supercond, 2001, 351: 103–117

64 Ando Y, Komiya S, Segawa K, et al. Electronic phase diagram of high-T_c cuprate superconductors from a mapping of the in-plane resistivity curvature. Phys Rev Lett, 2004, 93: 267001

65 Liang R, Bonn D A, Hardy W N, et al. Lower critical field and superfluid density of highly underdoped $YBa_2Cu_3O_{6+x}$ single crystals. Phys Rev Lett, 2005, 94: 117001

66 Inam A, Wu X D, Nazar L, et al. Microwave properties of highly oriented $YBa_2Cu_3O_{7-x}$ thin films. Appl Phys Lett, 1990, 56: 1178–1180

67 Arpaia R, Andersson E, Trabaldo E, et al. Probing the phase diagram of cuprates with $YBa_2Cu_3O_{7-\delta}$ thin films and nanowires. Phys Rev Mater, 2018, 2: 024804

68 Likharev K K. Superconducting weak links. Rev Mod Phys, 1979, 51: 101–159

69 Fagaly R L. Superconducting quantum interference device instruments and applications. Rev Sci Instruments, 2006, 77: 101101

70 Zheng D N. Superconducting quantum interference devices. Acta Phys Sin, 2021, 70: 018502

71 Pfeiffer C, Ruffieux S, Jonsson L, et al. A 7-channel high-T_c SQUID-based on-scalp MEG system. IEEE Trans Biomed Eng, 2019, 67: 1483–1489

72 Andersen L M, Pfeiffer C, Ruffieux S, et al. On-scalp MEG SQUIDs are sensitive to early somatosensory activity unseen by conventional MEG. NeuroImage, 2020, 221: 117157

73 Foley C P, Leslie K E, Binks R A. A history of the CSIRO's development of high temperature superconducting RF SQUIDs for TEM prospecting. ASEG Extended Abstracts, 2006. 1–5

74 Seidel P. Applied Superconductivity: Handbook on Devices and Applications. New Jersey: John Wiley & Sons, 2015

75 Stolz R, Schmelz M, Zakosarenko V, et al. Superconducting sensors and methods in geophysical applications. Supercond Sci Technol, 2021, 34: 033001

76 Wu J, Chen X, Yang Y, et al. Application of TEM based on HTS SQUID magnetometer in deep geological structure exploration in the baiyun gold deposit, NE China. J Earth Sci, 2021, 32: 1–7

77 Krause H J, Kreutzbruck M. Recent developments in SQUID NDE. Physica C-Supercond, 2002, 368: 70–79

78 De Wolf I, Jacobs K J P, Orozco A. Magnetic field imaging and light induced capacitance alteration for failure analysis of Cu-TSV interconnects. MicroElectron Reliability, 2020, 114: 113780

79 Schultze V, IJsselsteijn R, Boucher R, et al. Improved high-T_c superconducting quantum interference filters for sensitive magnetometry. Supercond Sci Technol, 2003, 16: 1356–1360

80 Caputo P, Oppenländer J, Häussler C, et al. High-performance magnetic field sensor based on superconducting quantum interference filters. Appl Phys Lett, 2004, 85: 1389–1391

81 Oppenlaender J, Haeussler C, Friesch A, et al. Superconducting quantum interference filters operated in commercial miniature cryocoolers. IEEE Trans Appl Supercond, 2005, 15: 936–939

82 Schultze V, IJsselsteijn R, Meyer H G. How to puzzle out a good high-T_c superconducting quantum interference filter. Supercond Sci Technol, 2006, 19: S411–S415

83 Cybart S A, Wu S M, Anton S M, et al. Series array of incommensurate superconducting quantum interference devices from $YBa_2Cu_3O_{7-\delta}$ ion damage Josephson junctionss. Appl Phys Lett, 2008, 93: 182502

84 Ouanani S, Kermorvant J, Crété D G, et al. HTS ion damage Josephson junction technology for SQUID arrays. J Phys-Conf Ser, 2014, 507: 042008

85 Ouanani S, Kermorvant J, Ulysse C, et al. High-T_c superconducting quantum interference filters (SQIFs) made by ion irradiation. Supercond Sci Technol, 2016, 29: 094002

86 Pawlowski E R, Kermorvant J, Crété D, et al. Static and radio frequency magnetic response of high T_c superconducting quantum interference filters made by ion irradiation. Supercond Sci Technol, 2018, 31: 095005

87 Müller K H, Mitchell E E. Effect of junction critical current disorder in superconducting quantum interference filter arrays. Phys Rev B, 2024, 109: 054507

88 Mitchell E E, Hannam K E, Lazar J, et al. 2D SQIF arrays using 20 000 YBCO high R_n Josephson junctions. Supercond Sci Technol, 2016, 29: 06LT01

89 Kornev V K, Soloviev I I, Klenov N V, et al. Performance advantages and design issues of SQIFs for microwave applications. IEEE Trans Appl Supercond, 2009, 19: 916–919

90 LeFebvre J C, Cho E, Li H, et al. Flux focused series arrays of long Josephson junctions for high-dynamic range magnetic field sensing. J Appl Phys, 2022, 131: 163902

91 Du J, Gao X, Zhang T, et al. High-T_c superconducting quantum devices for cutting-edge terahertz technology. J Phys D-Appl Phys, 2025, 58: 313001

92 Gao X, Zhang T, Du J, et al. 340 GHz double-sideband mixer based on antenna-coupled high-temperature superconducting Josephson junction. IEEE Trans THz Sci Technol, 2019, 10: 21–31

93 Klushin A M, Lesueur J, Kampik M, et al. Present and future of high-temperature superconductor quantum-based voltage standards. IEEE Instrum Meas Mag, 2020, 23: 4–12

94 Klushin A M, He M, Levitchev M Y, et al. Optimization of the coupling of mm wave power to arrays of high-T_c Josephson junctions. J Phys-Conf Ser, 2008, 97: 012268

95 Gao X, Zhang T, Du J, et al. A dual-beam lens-free slot-array antenna coupled high-T_c superconducting fundamental mixer at the W-band. Supercond Sci Technol, 2021, 34: 125006

96 Gao X, Du J, Zhang T, et al. Noise and conversion performance of a high-T_c superconducting Josephson junction mixer at 0.6 THz. Appl Phys Lett, 2017, 111: 192603

97 Yao C, Chen Z, Ge J, et al. A compact 220 GHz heterodyne receiver module with planar Schottky diodes. AEU-Int J Electron Commun, 2018, 84: 153–161

98 Wang C, He Y, Lu B, et al. Robust sub-harmonic mixer at 340 GHz using intrinsic resonances of hammer-head filter and improved diode model. J Infrared Milli Terahz Waves, 2017, 38: 1397–1415

99 Treuttel J, Gatilova L, Maestrini A, et al. A 520–620-GHz Schottky receiver front-end for planetary science and remote sensing with 1070 K–1500 K DSB noise temperature at room temperature. IEEE Trans THz Sci Technol, 2015, 6: 148–155

100 Thomas B, Maestrini A, Gill J, et al. A broadband 835–900-GHz fundamental balanced mixer based on monolithic GaAs membrane Schottky diodes. IEEE Trans Microwave Theor Techn, 2010, 58: 1917–1924

101 Schlecht E, Siles J V, Lee C, et al. Schottky diode based 1.2 THz receivers operating at room-temperature and below for planetary atmospheric sounding. IEEE Trans THz Sci Technol, 2014, 4: 661–669

102 Zhou K M, Miao W, Geng Y, et al. Noise temperature distribution of superconducting hot electron bolometer mixers. Chin Phys B, 2020, 29: 058505

103 Silva J R, Laauwen W M, Mirzaei B, et al. 4× 2 Hot electron bolometer mixer arrays for detection at 1.4, 1.9 and 4.7 THz for a balloon borne terahertz observatory. In: SPIE Astronomical Telescopes + Instrumentation, 2024, Yokohama, Japan. Bellingham, Washington, USA: Proc SPIE, 2024. 131020I

104 Mirzaei B, Silva J R G, Vreeling W J, et al. Reduced noise temperatures of a THz NbN hot electron bolometer mixer. IEEE Trans THz Sci Technol, 2024, 15: 91–99

105 Zhang W, Miao W, Zhou K, et al. High sensitive THz superconducting hot electron bolometer mixers and transition edge sensors. In: SPIE/COS Photonics Asia, 2016, Beijing, China. Bellingham, Washington, USA: Proc SPIE, 2016. 1003009

106 Liu B L, Liu D, Yao M, et al. Terahertz high-sensitivity SIS mixer based on Nb-AlN-NbN hybrid superconducting tunnel junctions. Chin Phys B, 2024, 33: 058501

107 Rudakov K I, Khudchenko A V, Filippenko L V, et al. THz range low-noise SIS receivers for space and ground-based radio astronomy. Appl Sci, 2021, 11: 10087

108 Zhu H T, Liu D, Hu J, et al. Low-loss, thermally insulating, and flexible rectangular dielectric waveguide for sub-THz—Signal coupling in superconducting receivers. IEEE Trans THz Sci Technol, 2020, 10: 190–199

109 Jing Li, Takeda M, Zhen Wang M, et al. Characterization of the mixing performance of all-NbN superconducting tunnel junctions at 0.5 THz. IEEE Trans Appl Supercond, 2009, 19: 417–422

110 Kojima T, Kroug M, Takeda M, et al. Three quanta sensitivity superconductor–insulator–superconductor mixer for the 0.78–0.95 THz band. Appl Phys Express, 2009, 2: 102201

111 Bergeal N, Lesueur J, Faini G, et al. High T_c superconducting quantum interference devices made by ion irradiation. Appl Phys Lett, 2006, 89: 112515

112 Wen J G, Takagi T, Koshizuka N. Microstructural studies on YBCO film bicrystals with large single facet grain boundaries grown by liquid phase epitaxy. Supercond Sci Technol, 2000, 13: 820–826

113 Russek S E, Lathrop D K, Moeckly B H, et al. Scaling behavior of $YBa_2Cu_3O_{7-\delta}$ thin-film weak links. Appl Phys Lett, 1990, 57: 1155–1157

114 Poppe U, Divin Y Y, Faley M I, et al. Properties of $YBa_2Cu_3O_7$ thin films deposited on substrates and bicrystals with vicinal offcut and realization of high I_cR_n junctions. IEEE Trans Appl Supercond, 2002, 11: 3768–3771

115 Mitchell E E, Foley C P. YBCO step-edge junctions: influence of morphology on junction transport. IEEE Trans Appl Supercond, 2011, 21: 371–374

116 Foley C P, Mitchell E E, Lam S K H, et al. Fabrication and characterisation of YBCO single grain boundary step edge junctions. IEEE Trans Appl Supercond, 2002, 9: 4281–4284

117 Mitchell E E, Foley C P. YBCO step-edge junctions with high I_cR_n. Supercond Sci Technol, 2010, 23: 065007

118 Kaczmarek L L, IJsselsteijn R, Zakosarenko V, et al. Advanced HTS DC SQUIDs with step-edge Josephson junctions for geophysical applications. IEEE Trans Appl Supercond, 2018, 28: 1–5

119 Faley M I, Slobodchikov V Y, Maslennikov Y V, et al. High-T_c dual-SQUIDs with graphoepitaxial step-edge junctions. IEEE Trans Appl Supercond, 2016, 26: 1–4

120 Faley M I, Poppe U, Dunin-Borkowski R E, et al. High-T_c DC SQUIDs for magnetoencephalography. IEEE Trans Appl Supercond, 2012, 23: 1600705

121 Ono R H, Beall J A, Cromar M W, et al. High-T_c superconductor-normal metal-superconductor Josephson microbridges with high-resistance normal metal links. Appl Phys Lett, 1991, 59: 1126–1128

122 Reintsema C D, Ono R H, Barnes G, et al. The critical current and normal resistance of high-T_c step-edge SNS junctions. IEEE Trans Appl Supercond, 1995, 5: 3405–3409

123 Grove M, Dittmann R, Bode M, et al. Current transport across $YBa_2Cu_3O_7$–Au interfaces. Appl Phys Lett, 1996, 69: 696–698

124 Wakana H. Development of thin film multilayer structures with smooth surfaces for HTS SFQ circuits. IEICE Trans Electron, 2005, E88-C: 208–215

125 Wakana H, Adachi S, Kamitani A, et al. Improvement in reproducibility of multilayer and junction process for HTS SFQ circuits. IEEE Trans Appl Supercond, 2005, 15: 153–156

126 Tian L F, Liu P, Meng X M. Research progress on helium ion microscope (in Chinese). J Chin Electron Microsc Soc, 2022, 41: 673–684 [田利丰, 刘培, 孟祥敏. 氦离子显微镜的发展及现状. 电子显微学报, 2022, 41: 673–684]

127 Chen D, Qiao R, Xu X, et al. Sub-10 nm stable graphene quantum dots embedded in hexagonal boron nitride. Nanoscale, 2019, 11: 4226–4230

128 Cybart S A, Cho E Y, Wong T J, et al. Nano Josephson superconducting tunnel junctions in $YBa_2Cu_3O_{7-\delta}$ directly patterned with a focused helium ion beam. Nat Nanotech, 2015, 10: 598–602

129 Müller B, Karrer M, Limberger F, et al. Josephson junctions and SQUIDs created by focused helium-ion-beam irradiation of $YBa_2Cu_3O_7$. Phys Rev Appl, 2019, 11: 044082

130 Karrer M, Wurster K, Linek J, et al. Temporal evolution of electric transport properties of $YBa_2Cu_3O_{7-\delta}$ Josephson junctions produced by focused-helium-ion-beam irradiation. Phys Rev Appl, 2024, 21: 014065

131 Cho E Y, Ma M K, Huynh C, et al. $YBa_2Cu_3O_{7-\delta}$ superconducting quantum interference devices with metallic to insulating barriers written with a focused helium ion beam. Appl Phys Lett, 2015, 106: 252601

132 Li H, Cai H, Cho E Y, et al. High-transition-temperature nanoscale superconducting quantum interference devices directly written with a focused helium ion beam. Appl Phys Lett, 2020, 116: 070601

133 Forman J, Yoshizumi S, Cai H, et al. High-T_c superconducting quantum interference device implemented on a pulsed tube cooler for 1 to 50 K materials characterization. IEEE Trans Appl Supercond, 2023, 33: 1–4

134 Cai H, LeFebvre J C, Li H, et al. High-temperature superconductor quantum flux parametron for energy efficient logic. Appl Phys Lett, 2024, 124: 212601

135 Cai H, Li H, Cho E Y, et al. $YBa_2Cu_3O_{7-\delta}$ single flux quantum flip flop directly written with a focused helium ion beam. IEEE Trans Appl Supercond, 2021, 31: 1–5

136 Cortez A T, Cho E Y, Li H, et al. Tuning Y–Ba–Cu–O focused helium ion beam Josephson junctions for use as THz mixers. IEEE Trans Appl Supercond, 2019, 29: 1–5

137 Schmid C, Jozani A, Kleiner R, et al. $YBa_2Cu_3O_7$ Josephson diode fabricated by focused-helium-ion-beam irradiation. Phys Rev Appl, 2025, 24: 014041

138 Li H, Cai H, Cho E Y, et al. $YBa_2Cu_3O_{7-\delta}$ nano-SQUIDs fabricated by focused helium ion beam direct writing. In: Proceedings of the 2019 IEEE International Superconductive Electronics Conference, 2019. 1–3

139 Li H, Cai H, Sarkar N, et al. Arrays of nano-high-transition temperature superconductor quantum interference devices. Appl Phys Lett, 2024, 124: 192603

140 Li Z, Ma H, Huang J, et al. Minimal lateral damage fabrication of high-temperature superconducting nanowires via focused helium ion beam irradiation. Supercond Sci Technol, 2024, 37: 125010

141 Hayashi K, Ohtani R, Tottori Y, et al. Study of HTS nanobridge Josephson junctions made by FIB. IEEE Trans Appl Supercond, 2022, 32: 1–6

142 Chen Z, Li Y, Zhu R, et al. High-temperature superconducting $YBa_2Cu_3O_{7-\delta}$ Josephson junction fabricated with a focused helium ion beam. Chin Phys Lett, 2022, 39: 077402

143 Chen Z, Zhang Y, Ma P, et al. Co-doped $BaFe_2As_2$ Josephson junction fabricated with a focused helium ion beam. Chin Phys B, 2024, 33: 047405

144 Wang X, Chen F, Lin Z, et al. On the path to high-temperature Josephson multi-junction devices. Electromagn Sci, 2024, 2: 1–8

145 Yin D, Cai X, Xu T, et al. MgB_2 Josephson Junctions fabricated by Focused Helium Ion Beam with different irradiation doses on SiC and MgO substrates. Physica C-Supercond its Appl, 2024, 623: 1354532

146 Yin D, Cai X, Xu T, et al. Half-integer Shapiro steps in MgB_2 focused He ion beam Josephson junctions. Chin Phys B, 2024, 33: 087404

147 Wakana H, Adachi S, Tsubone K, et al. Fabrication of high-temperature superconductor single-flux-quantum circuits using a multilayer structure

with a smooth surface. Supercond Sci Technol, 2006, 19: S312–S315
148 Francke C, Krämer A, Offner M, et al. Ion-beam etching of substrate steps: SNS compared to step-edge grain boundary Josephson-junctions. Appl Supercond, 1999, 6: 735–739
149 Koelle D, Kleiner R, Ludwig F, et al. High-transition-temperature superconducting quantum interference devices. Rev Mod Phys, 1999, 71: 631–686
150 Adachi S, Tsukamoto A, Oshikubo Y, et al. Fabrication of HTS ramp-edge-type Josephson junctions and SQUIDs using various YBCO-derivatives as barrier materials. Jpn J Appl Phys, 2021, 60: 093001

补充材料

表S1 图5(a), (b)中SQIF数据总结
表S2 图5(c)中太赫兹混频器数据总结

本文以上补充材料见网络版csb.scichina.com. 补充材料为作者提供的原始数据, 作者对其学术质量和内容负责.

Summary for “钇钡铜氧薄膜与约瑟夫森结研究进展”

Research progress on $YBa_2Cu_3O_{7-\delta}$ thin films and Josephson junctions

Ji-Quan Zhang[1], Fu-Cong Chen[1*], Xiao-Ping Ma[1], Dan Qiao[2], Yu-Tong Wang[1], Jing-Ting Yang[3], Zhong-Pei Feng[3], Zhong-Hua Bai[1], Pei-Yu Xiong[3], Jia-Xiao Wang[1], Chun-Gunag Li[1], Huai-Xin Yang[1], Qian Li[1], Shi-Bing Tian[1], Xiang Gao[2], Yue Wang[4], Xu Wang[1*], Jie Yuan[1], Bei-Yi Zhu[1] & Kui Jin[1]

[1] *Institute of Physics, Chinese Academy of Sciences, Beijing 100190, China*
[2] *School of Cyberspace Science and Technology, Beijing Institute of Technology, Beijing 100081, China*
[3] *Songshan Lake Materials Laboratory, Dongguan 523808, China*
[4] *School of Physics, Peking University, Beijing 100871, China*
* Corresponding authors, E-mail: fucong@iphy.ac.cn; risingsunwx@iphy.ac.cn

High-temperature superconducting (HTS) $YBa_2Cu_3O_{7-\delta}$ (YBCO) thin films and Josephson junctions are pivotal for both fundamental research into HTS mechanisms and practical electronic devices operating at liquid nitrogen temperatures. This article provides a comprehensive review of recent advances in the fabrication techniques, physical properties, and applications status of YBCO thin films and Josephson junctions, describing the path from fundamental research toward technological implementation.

Substantial progress has been made in the growth of YBCO thin films. Advanced deposition methods, including pulsed laser deposition (PLD), magnetron sputtering, and metal-organic chemical vapor deposition (MOCVD), have enabled the production of films with enhanced superconducting properties over large areas. Critical parameters such as the superconducting transition temperature (T_c), critical current density (J_c), and surface smoothness have seen continuous improvement. Through strategies such as substrate strain, the use of buffer layers (e.g., CeO_2), the construction of superlattices (e.g., $PrBa_2Cu_3O_7$/YBCO), and annealing with active oxygen sources, researchers can effectively suppress twinning rate, control oxygen doping homogeneity, and modulate electronic structures. These capabilities are indispensable not only for probing fundamental phenomena like the pseudogap phase and charge density waves but also for meeting the exacting material specifications required for high-performance devices. Nevertheless, challenges persist. The microwave surface resistance (R_s) of even the best films, while far superior to conventional metals, has not yet reached its theoretical minimum.

Great achievements have been realized in the fabrication of YBCO Josephson junctions, the fundamental building blocks of HTS electronics. Superconducting quantum interference filters (SQIFs), comprising arrays of junctions, exhibiting an improved range of single-valued and linear range of the magnetic field-voltage response, enable highly sensitive absolute magnetometry. The high-temperature superconducting terahertz mixer utilizes the nonlinear current-voltage characteristics of the Josephson junction to achieve frequency conversion of microwave/terahertz signals. Compared to other types, it has the potential for lower noise temperature and a lighter cooling system. Series arrays of thousands of junctions are also being developed for a voltage standard through alternating current Josephson effect. Furthermore, the phase-sensitive technique of YBCO untwinned thin films and Josephson junctions provides crucial evidence for revealing the pairing symmetry of HTS materials.

The community has developed a variety of methods for preparing Josephson junctions, and each technique has its own unique characteristics. Bi-crystal junctions, defined by a grain boundary on a specially prepared substrate, offer a relatively simple and reproducible structure. Step-edge junctions, created by depositing YBCO over a lithographically defined substrate step, provide good design flexibility for individual devices. A step-edge SNS junction is formed by depositing metal on the steeper steps, as the junction region contracts with grain boundaries. Inclined-edge junctions have excellent stability and anti-interference capabilities with top electrodes. In particular, the emergence of focused helium ion beam (He-FIB) technology represents a breakthrough. This direct-write technique with a high degree of freedom utilizes a sub-nanometer helium ion probe to locally modify the oxygen content or crystal structure, creating a tunable barrier within the range limited by the superconducting coherence length. Its greatest strength lies in enabling the fabrication of large-scale, dense arrays of junctions with complex geometries, a capability important for integrated devices.

Despite these promising developments, critical challenges should be addressed to achieve industrialization and commercialization. For junction arrays, the statistical scatters in key parameters like critical current (I_c) and normal resistance (R_n) need further optimization for device stability and reproducibility. Future progress depends on a co-optimization strategy: advancing film growth to achieve outstanding and homogeneous superconducting performance and perfect surface flatness; minimizing damage and improving uniformity in nanofabrication processes of junctions; establishing microstructure-function relationships to guide empirical optimization with physical insight.

high-temperature superconductivity, YBCO, thin film, Josephson junction, electronics device, focused helium ion beam

doi: 10.1360/CSB-2025-5615